



**HAL**  
open science

## **Thermal evolution of a metal drop falling in a less dense, more viscous fluid**

B. Qaddah, Julien Monteux, M. Le Bars

### ► **To cite this version:**

B. Qaddah, Julien Monteux, M. Le Bars. Thermal evolution of a metal drop falling in a less dense, more viscous fluid. *Physical Review Fluids*, 2020, 5, pp.053801. <10.1103/PhysRevFluids.5.053801>. <hal-02563299>

**HAL Id: hal-02563299**

**<https://hal.science/hal-02563299v1>**

Submitted on 5 May 2020

**HAL** is a multi-disciplinary open access archive for the deposit and dissemination of scientific research documents, whether they are published or not. The documents may come from teaching and research institutions in France or abroad, or from public or private research centers.

L'archive ouverte pluridisciplinaire **HAL**, est destinée au dépôt et à la diffusion de documents scientifiques de niveau recherche, publiés ou non, émanant des établissements d'enseignement et de recherche français ou étrangers, des laboratoires publics ou privés.



HAL Authorization

1 Thermal evolution of a metal drop falling in a less  
2 dense, more viscous fluid

3 B. Qaddah<sup>a,b</sup>, J. Monteux<sup>b</sup>, M. Le Bars<sup>a</sup>

4 <sup>a</sup>*CNRS, Aix Marseille Univ, Centrale Marseille, IRPHE, Marseille, France*

5 <sup>b</sup>*Université Clermont Auvergne, CNRS, IRD, OPGC, Laboratoire Magmas et Volcans,*  
6 *F-63000 Clermont-Ferrand, France*

7 *Corresponding author: qaddah@irphe.univ-mrs.fr*

---

8 **Abstract**

9 The initial state of terrestrial planets was partly determined, during accretion,  
10 by the fall of metal drops in a liquid magma ocean. Here, we perform systematic  
11 numerical simulations in 2D cylindrical axisymmetric geometry of these falling  
12 dynamics and associated heat exchanges at the scale of one single drop, for var-  
13 ious initial sizes and ambient viscosities. We explore Reynolds number in the  
14 range  $[0.05 - 48]$ , viscosity ratios in the range  $[50 - 4000]$ , Weber number in the  
15 range  $[0.04 - 5]$  and Peclet number in the range  $[70 - 850]$ . We show that heat  
16 exchanges between the two phases occurs predominantly at the front section  
17 of the drop. Our systematic, parametric study exhibits shows that the ther-  
18 mal boundary layer thickness, the depth and time for equilibration, the Nusselt  
19 number, and the magma ocean volume affected by thermal echanges, all scale  
20 as power laws of the Peclet number. Because of drop distortions, these scaling  
21 laws deviate from the classical balances considering only heat diffusion through  
22 a laminar thermal boundary layer. Finally, when considering a temperature-  
23 dependent viscosity of the ambient fluid, we show that a low viscosity layer  
24 surrounds the drop, which influences the thermal evolution of non-deformable,  
25 low Reynolds number drops only, and decreases the breakup distance for some  
26 limited breakup modes.

28 *Keywords:* Core formation, drop dynamics, thermal exchanges, two-phase  
29 flow, numerical modeling.

---

## 30 **1. Introduction**

31 Core formation of terrestrial planets is a complex process contemporaneous  
32 with planetary accretion (1; 2). Its fluid dynamics and thermodynamics have  
33 been addressed in numerous studies (e.g. 3; 4; 5; 6; 7; 8). During the last stages  
34 of e.g. Earth accretion, giant impacts likely occurred between the proto-Earth  
35 and up to Mars-sized differentiated bodies (9). The kinetic energy released dur-  
36 ing such collisions (10; 11), the radioactive heating caused by the disintegration  
37 of short-lived radio-elements (12), and the heat dissipation resulting from the  
38 conversion of potential energy during core formation and core/mantle separa-  
39 tion (13), melt part or all of the Earth mantle (10). Following each impact, the  
40 iron core of the impactor thus spreaded and sank into a deep magma ocean.  
41 There, the metal further fragmented into drops and diapirs of different sizes,  
42 ranging from millimeter drops up to maybe kilometers diapirs, before assem-  
43 bling with the Earth proto-core ((5; 7; 14; 15)). Thermochemical exchanges  
44 occurred between the fragmented metal drops and the liquid magma ocean dur-  
45 ing their sinking, determining the initial thermal and chemical state of the planet  
46 ((16; 17; 18; 5)). Past studies have provided many scenarios to characterize and  
47 quantify the thermochemical exchanges. (16) and (19) modelled the diffusive  
48 equilibration through a laminar thermal boundary layer of respectively, a cloud  
49 of uniform drops and a large diapir of iron. (18) further evaluated the influence  
50 of drop deformations in (16) scenario. (20) solved the fully coupled dynamical  
51 and thermal/chemical equations, but for a fixed spherical geometry only. (5)  
52 used experiments where a large volume of immiscible fluid falls into a less dense  
53 ambient to show that the smallest scale of turbulence – rather than diffusion

54 through a laminar boundary layer – leads to rapid thermo-chemical equilibra-  
55 tion, even before fragmentation. (8) confirmed this conclusion in their analog  
56 model, measuring the global cooling of a large volume of hot Galinstan after its  
57 fall through a deep tank of viscous oil. Yet a systematic temporal description of  
58 heat exchanges at the scale of one falling, freely evolving drop, is still missing.

59 Importantly, the magma ocean viscosity highly depends on its evolving tem-  
60 perature and pressure (21). Therefore, the viscosity ratio between the magma  
61 ocean and iron drops can vary by several orders of magnitude as a function of  
62 depth, of time after impact, etc. Following and extending an abundant literature  
63 in different contexts (e.g. 22; 23; 24; 25; 26), analog experiments by (7; 8) and  
64 numerical simulations at the scale of one metal drop by (27) showed that the vis-  
65 cosity contrast indeed plays an important role in iron drops shape, velocity and  
66 fragmentation. (27) predicted that thermo-chemical exchanges should increase  
67 with drop deformation and oscillations; but they did not explicitly solve for  
68 the fully coupled dynamical and thermal equations. This is the purpose of the  
69 present paper. Open questions include: How and where do heat exchanges oc-  
70 cur? Do the drop deformation/oscillations indeed favor heat exchanges? What  
71 are the characteristics time and depth needed to reach equilibration between the  
72 two phases? And, what is the influence of a temperature dependent viscosity of  
73 the magma?

74 The paper is organised as follows. Section 2 introduces the physical and  
75 numerical models, with the governing equations, the non-dimensional parame-  
76 ters, and the numerical method. Section 3 presents in detail a reference case,  
77 describing its mechanical and thermal behavior, average temperature evolu-  
78 tion, heat transfer at the drop interface, and the magma ocean volume heated  
79 during the drop sinking. In Section 4, we present the main numerical results  
80 from our systematic parametric study, and derive generic scaling laws for the

81 above detailed parameters. Section 5 then focuses on changes induced by a  
 82 temperature-dependent viscosity in the magma ocean. Conclusions and future  
 83 works are outlined in final section 6.

## 84 **2. Physical and numerical models**

### 85 *2.1. Governing equations*

86 We consider an initially spherical, liquid metal drop of radius  $R$ , falling  
 87 in an initially motionless, less dense and more viscous surrounding fluid (i.e.  
 88 a magma ocean) under the action of gravity. The initial temperature of the  
 89 liquid drop and of the magma ocean strongly depends on the growth history  
 90 of the protoplanet before the impact and on its initial heating caused by short  
 91 lived elements (13). Here, we consider that the liquid metal drop is hotter  
 92 than the magma ocean, with uniform initial temperatures in both phases. Both  
 93 phases behave as Newtonian, incompressible, and immiscible fluids with uniform  
 94 surface tension, and constant density and viscosity within each fluid at first.  
 95 Later on in section 5, we also consider a temperature dependent magma ocean  
 96 viscosity. The dynamical and thermal evolution of the falling drop and ambient  
 97 liquid is governed by the Navier-Stokes and heat transfer equations, describing

- 98 • The mass conservation:

$$\nabla \cdot \mathbf{u} = 0, \quad (1)$$

99 with  $\mathbf{u}$  the fluid velocity vector ( $\text{m}\cdot\text{s}^{-1}$ ).

- 100 • The momentum conservation:

$$\rho \left( \frac{\partial \mathbf{u}}{\partial t} + \mathbf{u} \cdot \nabla \mathbf{u} \right) = \nabla \cdot [-P\mathbf{I} + \mu(\nabla \mathbf{u} + (\nabla \mathbf{u})^T)] + \rho \mathbf{g} + \mathbf{F}_{st} \quad (2)$$

101 with  $\rho$  the fluid density ( $\text{kg}\cdot\text{m}^{-3}$ ),  $\mu$  the fluid dynamic viscosity (Pa.s),  $t$   
 102 the time (s),  $P$  the fluid pressure (Pa),  $\mathbf{g}$  the gravitational acceleration  
 103 ( $\text{m}\cdot\text{s}^{-2}$ ),  $\mathbf{F}_{st}$  the surface tension force ( $\text{N}\cdot\text{m}^{-3}$ ) and  $\mathbf{I}$  the identity matrix.

104 • The heat conservation:

$$\rho C_p \left[ \frac{\partial T}{\partial t} + \mathbf{u} \cdot \nabla T \right] + \nabla \cdot [-k \nabla T] = 0 \quad (3)$$

105 with  $C_p$  the heat capacity at constant pressure ( $\text{J}\cdot\text{kg}^{-1}\cdot\text{K}^{-1}$ ),  $T$  the fluid  
 106 temperature (K),  $k$  the fluid thermal conductivity ( $\text{W}\cdot\text{m}^{-1}\cdot\text{K}^{-1}$ ). No heat  
 107 source is considered in our model. We ignore the effect of viscous dissi-  
 108 pation in this work as we study droplets on small scales of millimetres to  
 109 centimetres. The absence of viscous dissipation for these studied drops  
 110 does not affect the thermal evolution in the system.

111 To monitor the interface between the falling drop and the magma ocean,  
 112 we use the Level Set method, an Eulerian and implicit method frequently used  
 113 in multiphase flow problems (e.g. 28). The Level Set function  $\phi$  equals to 1 in  
 114 the metal drop and 0 in the ambient liquid, and rapidly changes through the  
 115 interface, whose position is determined by the isocontour  $\phi = 0.5$ . The transport  
 116 and reinitialization of the Level Set function  $\phi$  are governed by:

$$\frac{\partial \phi}{\partial t} + \mathbf{u} \cdot \nabla \phi = \gamma \nabla \cdot \left[ \epsilon \nabla \phi - \phi(1 - \phi) \frac{\nabla \phi}{|\nabla \phi|} \right] \quad (4)$$

117 with  $\gamma$  (m/s) and  $\epsilon$  (m) the reinitialization parameters.  $\gamma$  determines the reini-  
 118 tialization amount: a suitable value for  $\gamma$  is the maximum velocity magnitude  
 119 experienced in the model.  $\epsilon$  determines the layer thickness around the interface,  
 120 and is equal to half the size of the characteristic mesh in the region explored by  
 121 the interface. The density and dynamical viscosity are evaluated using the level  
 122 set function:

$$\rho = \rho_m + (\rho_d - \rho_m)\phi \quad (5)$$

123

$$\mu = \mu_m + (\mu_d - \mu_m)\phi \quad (6)$$

124 where subscripts “m” and “d” stand for the magma ocean and the liquid metal  
 125 drop, respectively. The surface tension force is determined by :

$$\mathbf{F}_{st} = \nabla \cdot \mathbf{T} = \nabla \cdot (\sigma[\mathbf{I} + (-\mathbf{n}\mathbf{n}^T)]\delta) \quad (7)$$

126 with  $\sigma$  (N/m) the surface tension coefficient,  $I$  the identity matrix,  $\mathbf{n}$  the in-  
 127 terface normal unit vector, and  $\delta$  the Dirac delta function, nonzero only at the  
 128 fluid interface. The interface normal unit vector is calculated as

$$\mathbf{n} = \frac{\nabla\phi}{|\nabla\phi|}. \quad (8)$$

129 The level set parameter  $\phi$  is also used to approximate the delta function by a  
 130 smooth function (29) defined by

$$\delta = 6 |\phi(1 - \phi)| |\nabla\phi|. \quad (9)$$

131 Note that in this work we do not calculate the chemical exchanges between  
 132 the two phases. Instead, the main difference between the heat and mass transfer  
 133 equations, if the thermal and chemical sources are neglected, is the partition  
 134 coefficient between the two phases (30). When the partition coefficient is equal  
 135 to 1, we can use the results of this study in geochemical models of planet building  
 136 (31).

## 137 2.2. Physical and non-dimensional parameters

138 The main parameters that characterize the dynamical and thermal evolution  
 139 of a falling drop in a more viscous medium are the viscosity, density, thermal

140 conductivity, heat capacity and initial temperature of the two fluids, the initial  
 141 drop size, the gravity, and the surface tension between the two phases. In the  
 142 geophysical problem of interest (i.e. core formation), the magma ocean viscosity  
 143 and the metal drop initial radius vary over a wide range of values, while the other  
 144 parameters are roughly constant (even if rigorously, the thermal conductivity  
 145 and heat capacity of a magma ocean moderately depend on its composition  
 146 (e.g. 32; 33), and the thermal conductivity and heat capacity of metal drops  
 147 moderately depend on temperature and pressure (e.g. 34; 35)). Hence in this  
 148 study, we vary these two parameters  $R$  and  $\mu_m$ , in the accessible, relevant ranges  
 149 4–25 mm and 0.25–20 Pa.s respectively, while we keep all the other parameters  
 150 fixed at their representative geophysical values (see Table 1).

Table 1: Symbol definitions and values of the physical and non-dimensional parameters used in this study.

	Symbol	Value or range
Magma ocean density	$\rho_m$	3500 kg/m <sup>3</sup>
Metal drop density	$\rho_d$	7500 kg/m <sup>3</sup>
Metal drop viscosity	$\mu_d$	0.005 Pa.s
Magma ocean viscosity	$\mu_m$	0.25 - 20 Pa.s
Initial drop radius	$R$	4 - 25 mm
Surface tension coefficient	$\sigma$	1 N/m
Magma ocean heat capacity	$Cp_m$	667 J.kg <sup>-1</sup> .K <sup>-1</sup>
Metal heat capacity	$Cp_d$	800 J.kg <sup>-1</sup> .K <sup>-1</sup>
Magma ocean conductivity	$k_m$	10 W.m <sup>-1</sup> .K <sup>-1</sup>
Metal conductivity	$k_d$	100 W.m <sup>-1</sup> .K <sup>-1</sup>
Viscosity ratio	$R_\mu$	50 - 4000
Density ratio	$R_\rho$	2.14
Reynolds number	$Re$	0.05 - 48
Weber number	$We$	0.04 - 5
Peclet number	$Pe$	70 - 850
Nusselt number	$Nu$	1 - 6

151 In our simulations, the drop falls from rest, accelerates until reaching a con-  
 152 stant terminal velocity, possibly with small oscillations around it, and thermally

153 exchanges heat with the ambient liquid. We pursue continue our simulations  
 154 until the drop reaches a stable dynamical regime and its temperature contrast  
 155 with the ambient reaches less than 20% of its initial value. During the fall, we  
 156 monitor the average terminal velocity  $V$  and the average temperature  $T$  of the  
 157 drop (minus the initial ambient temperature). The dynamical and thermal evo-  
 158 lution of each drop is then characterised by the following output dimensionless  
 159 numbers:

- 160 • the Reynolds number ( $Re = \frac{\rho_m V R}{\mu_m}$ ) is the ratio of inertial to viscous  
 161 forces. Three different regimes are possible: the Stokes regime corresponds  
 162 to  $Re < 1$  where the viscous effects dominate; the Intermediate regime  
 163 corresponds to  $Re = 1 - 500$  where both viscous and inertial forces are  
 164 important; and the Newtonian regime corresponds to  $Re > 500$  where the  
 165 inertial forces are dominant. Here, the Reynolds number ranges from 0.05  
 166 to 48, hence our drops are in the Stokes to Intermediate regime.
- 167 • the Weber number ( $We = \frac{\rho_m V^2 R}{\sigma}$ ) compares the inertial and surface ten-  
 168 sion forces. It governs the deformation, breakup and terminal shape of  
 169 a drop (see e.g. 36; 27). When  $We < O(1)$ , the drop remains spherical  
 170 without any change of its morphology, while increasing Weber number  
 171 leads to stronger and stronger deformation, then to fragmentation above  
 172 a threshold which increases with the viscosity ratio, starting from  $\sim 3$  for  
 173 viscosity ratio  $\leq 1$  (see e.g. 37; 27). Here, the Weber number ranges from  
 174 0.04 to 5, considering stable, potentially deformable drops only.
- 175 • the Peclet number ( $Pe = \frac{\rho_m C_p V R}{k_m}$ ) compares the rate of heat advection  
 176 to diffusion at the drop scale. Here, the Peclet number ranges from 70 to  
 177 850, so heat transfers are strongly affected by advection.
- 178 • the Nusselt number ( $Nu = \frac{R \bar{\nabla} T \cdot \mathbf{n}}{(T_{int} - T_m)}$ ) compares the measured, averaged

179 heat transfer at the drop interface to a purely conductive case, with  $\overline{T_{int}}$   
180 the mean temperature at the interface and  $T_m$  the magma ocean temper-  
181 ature far from the drop. Here, the Nusselt number ranges from 1 to 6,  
182 hence confirming the important role of advection in heat transfers.

183 All relevant parameter values are given in Table 1.

### 184 *2.3. Numerical model*

185 We solve Eqs. (1 - 4) using axisymmetric simulations with the COMSOL  
186 Multiphysics software, based on the finite element method. The details of our  
187 17 runs for this study are listed in Table 2. Each run represents 2 to 4 weeks  
188 computation time on a bi-processor, eight-core, 3.2 – 3.6 GHz workstation. The  
189 axisymmetric geometry assumption is validated by (38) for a Weber number  
190 up to 120. For the dynamics, we use open conditions at the top and bottom  
191 boundaries and no-slip conditions at the lateral boundary. For the temperature,  
192 we consider no flux conditions at all boundaries. The computational domain  
193 must be large enough to allow for convergence without any wall effects. Here,  
194 we chose an axisymmetric cylinder of size  $(r \times z) = (12R \times 200R)$ , which is  
195 sufficiently large to reach a statistically steady motion (see our previous study  
196 (27)) and to follow equilibration up to a 80% decrease of the initial temperature  
197 anomaly.

198 To capture precisely the dynamical and thermal evolution of the drop, a fine  
199 mesh is required. For that, we use an adaptive mesh with a high resolution  
200 in the drop vicinity. As shown in figure 1, we divide our domain into several  
201 regions where the cell sizes vary between  $h = 0.015R$  to  $h = 1.5R$ . As detailed  
202 in (27), the simulation is programmed to stop when the drop reaches the bottom  
203 of the finest mesh region: the whole mesh pattern is then translated and the  
204 simulation is restarted on this new grid (see Figure 1 Right).

Table 2: Dimensional and non-dimensional parameters for all performed simulations used in this study.  $Pe_h$  is the grid Peclet number (see section 2.3).

<i>Simulation</i>	$R(mm)$	$\mu_m(Pa.s)$	$R_\mu$	$Re$	$We$	$Pe$	$Pe_h$	$\Delta T(K)$
#1	8	20	4000	0.05	0.04	70	0.43	100
#2	8	10	2000	0.2	0.15	137.26	0.84	100
#3	8	5	1000	0.76	0.52	254	1.55	100
#3a ( $T$ dependent $\mu_m$ )	8	5	1000	0.81	0.59	271	1.65	100
#3b ( $T$ dependent $\mu_m$ )	8	5	1000	0.98	0.85	327	2	1000
#4	8	1	200	9.5	3.23	635	3.89	100
#5	8	0.5	100	21.8	4.26	728.36	4.46	100
#5a ( $T$ dependent $\mu_m$ )	8	0.5	100	22.4	4.48	747.6	4.57	100
#5b ( $T$ dependent $\mu_m$ )	8	0.5	100	23.52	4.94	785	4.8	1000
#6	8	0.25	50	47.6	5	793.73	4.86	100
#6a ( $T$ dependent $\mu_m$ )	8	0.25	50	47.6	5	793.73	4.86	100
#6b ( $T$ dependent $\mu_m$ )	8	0.25	50	47.6	5	793.73	4.86	1000
#7	4	1	200	2.2	0.34	145.67	0.89	100
#8	6	1	200	5.67	1.53	378.19	2.32	100
#9	10	1	200	12.7	4.61	847.42	5.2	100
#10	25	1	200	45	23.2	3008	18.45	100
#10a ( $T$ dependent $\mu_m$ )	25	1	200	41.13	19.5	2745	16.8	1000

205 Mesh convergence has been checked. In (27), we showed that a mesh size  
206  $h = 0.025R$  (or smaller) allows to capture the falling drop dynamics. Here,  
207 we further performed two tests for the resolution of thermal transfers. In the  
208 first one, we compare the numerical and analytical heat transfers by thermal  
209 diffusion from a motionless spherical drop. The analytical solution for the radial  
210 temperature profile from the drop center to a given distance ( $r$ ) is given by (39)

$$T = 0.5T_0 \left[ \operatorname{erf} \frac{R+r}{2\sqrt{Dt}} + \operatorname{erf} \frac{R-r}{2\sqrt{Dt}} \right] - \frac{T_0}{r} \sqrt{\frac{Dt}{\pi}} \left[ e^{-\frac{(R-r)^2}{4Dt}} - e^{-\frac{(R+r)^2}{4Dt}} \right] \quad (10)$$

211 with  $T$  the temperature anomaly ( $T_0$  its initial value) and  $D$  the thermal diffu-  
212 sivity ( $m^2.s^{-1}$ ). Figure 2 (Left) shows the excellent agreement of our numerical  
213 results.

214 For the second test, we calculated, for different minimum grid sizes  $h =$   
 215  $0.05R, 0.035R, 0.025R, 0.015R, 0.01R$ , the normalized average drop temperature  
 216 as a function of normalized time for our reference case #4 in Table 2 (see  
 217 details in next section). Figure 2 (Right) shows a reasonable convergence of  
 218 the numerical results from  $h = 0.015R$ , with a relative maximum error  $\simeq 3.5\%$ ,  
 219 while the drop mass during the course of this simulation does not change by  
 220 more than 0.4% from its initial mass. Therefore, we confirm that our mesh  
 221  $h = 0.015R$  captures correctly the thermal evolution of the metal drop.

222 Finally, the grid Peclet number  $Pe_h = \frac{Vh}{D_{int}}$ , with  $D_{int} = \frac{D_d + D_m}{2}$  the mean  
 223 thermal diffusivity, is an appropriate parameter in the convection-diffusion equa-  
 224 tion to determine whether the heat transfer in the system corresponds to numer-  
 225 ical artifacts or not. (40) found very accurate solutions for grid Peclet number  
 226 up to 10. As shown in Table 2, our runs in this study remain below this crite-  
 227 rion for stability, except for run #10 which we hence do not consider for heat  
 228 transfer studies in the following sections.

### 229 3. Reference case

230 In this section, we present our reference case, from which, in the next section,  
 231 we then change the drop size keeping the viscosity ratio constant, and the magma  
 232 ocean viscosity keeping the drop size constant. This reference case corresponds  
 233 to simulation #4 in Table 2: the drop initial radius is 8 mm, the magma ocean  
 234 viscosity is 1 Pa.s, the metal viscosity is 0.005 Pa.s (viscosity contrast 200), and  
 235 the initial temperature difference between the metal drop and the magma ocean  
 236 is 100 K.

237 The drop motion from rest and its thermal evolution are shown in Figure 3.  
 238 The spherical drop accelerates due to gravity and rapidly deforms into a spher-  
 239 ical cap. Then, surface tension equilibrates inertia at the drop interface and

240 prevents any further change in morphology. Higher temperatures are concen-  
 241 trated at the front of the drop, while the thermal wake behind the drop expands  
 242 as a function of time. To characterize this dynamics, we define and compute  
 243 the following quantities.

### 244 3.1. Average ~~falling~~ drop velocity

245 During its fall, the drop mean velocity varies with time depending on the  
 246 drop morphology. In our simulations, we compute it as:

$$V(t) = \frac{\int_v U(r, z, t)[\phi(r, z, t) \geq 0.5]dv}{\int_v [\phi(r, z, t) \geq 0.5]dv} \quad (11)$$

247 with  $U(r, z, t)$  the local velocity magnitude (m/s),  $dv = 2\pi r dr dz$  accounting for  
 248 axisymmetric cylindrical geometry, and  $[\phi(r, z, t) \geq 0.5]$  the boolean operator  
 249 allowing to only capture the iron drop volume. Note that we use in this study  
 250 the mean magnitude velocity of drop which is very close to the average vertical  
 251 velocity (change of less than 3%). We normalise  $V(t)$  by the free fall Newton  
 252 velocity  $U_N = \sqrt{\frac{\Delta\rho g R}{\rho_m}}$  and time by the diffusion time  $t_{dif} = \frac{R^2 \rho_m C_{p_m}}{k_m}$ . Figure  
 253 4 shows the result for our reference case. The drop rapidly accelerates from rest  
 254 up to  $t^* = 0.02$ , then several small oscillations occur before reaching its asymp-  
 255 totic terminal fall velocity, which we use to compute the output dimensionless  
 256 numbers.

### 257 3.2. Average temperature evolution of the metal drop

258 As shown in Figure 3, the liquid drop ~~thermally~~ exchanges heat with the  
 259 liquid magma ocean and loses its heat as a function of time and depth. We  
 260 determine the mean average temperature anomaly of the drop compared to the  
 261 magma ocean as:

$$T(t) = \frac{\int_v T(r, z, t)[\phi \geq 0.5]dv}{\int_v [\phi \geq 0.5]dv} \quad (12)$$

262 We normalize  $T(t)$  by its initial value, giving  $T^*(t)$ . Its evolution for the refer-  
 263 ence case as a function of time or as a function of depth of its center of mass  
 264 (normalized by the initial radius  $R$ ) is shown in Figure 5. After a rapid adjust-  
 265 ment of the initial temperature jump at the interface,  $T^*$  decreases exponentially  
 266 towards equilibrium. We determine the best exponential fits according to

$$T^* = e^{(-t/t_c)} \quad \text{and} \quad T^* = C_z e^{(-z/l_c)} \quad (13)$$

267 where  $C_z$  is a constant (see Figure 5 in red color). In geophysical science, the  
 268 characteristic time ( $t_c$ ) and length ( $l_c$ ) for equilibration are very important pa-  
 269 rameters (8), used to set the degree of equilibration between iron and silicate of  
 270 magma ocean in planet building models (31). Note that chemical equilibrium  
 271 is more difficult to reach than thermal equilibrium because of its low diffusiv-  
 272 ity and is at least as important to planet formation as thermal equilibration,  
 273 especially for small metal volumes. Therefore, in the case of a partition coeffi-  
 274 cient between the two phases equal to 1, the results of this work can be used in  
 275 geochemical models of planet building.

### 276 *3.3. Volume of heated magma during the drop sinking*

277 The magma ocean temperature increases during the fall of the drop, espe-  
 278 cially in its wake. It is important in geophysics to quantify how much of the  
 279 magma is thermally affected by the formation of the iron core: this would for  
 280 instance affect the initial structure and heat budget of the Earth’s mantle. In  
 281 our simulations, we calculate the volume of magma ocean affected by thermal  
 282 exchange as:

$$V_o = \int_v [T > (T_m + T_C)][\phi \leq 0.5] dv \quad (14)$$

283 with  $T_C$  a chosen temperature anomaly ( $K$ ) and  $[\phi \leq 0.5]$  the boolean operator  
 284 allowing to only capture the magma ocean volume. An example of the captured

285 volume of heated magma ocean is shown in Figure 6 (Left). We performed  
 286 tests with several  $T_C$  corresponding to 0.1, 1 and 10 K. Results of the volume  
 287 normalized by the initial drop volume as a function of the drop depth are shown  
 288 in Figure 6 (Right). The three curves corresponding to different equilibrium  
 289 degrees are parallel, until a depth equals to 50R where  $T_C = 10$  K is strongly  
 290 affected by thermal diffusion in the magma ocean. The same behavior would of  
 291 course take place at longer time/depth for the other  $T_C$ . In the following, for  
 292 our parametric study, we compare heated volumes considering  $T_C = 1$  K and at  
 293 three different depths: 10, 20 and 30 R.

#### 294 *3.4. Heat transfer at the drop interface*

295 To evaluate the Nusselt number, we compute the mean temperature anomaly  
 296 and the mean temperature gradient at the interface, using respectively

$$\overline{T_{int}} = \frac{\int_v T\phi(1-\phi)dv}{\int_v \phi(1-\phi)dv} \quad (15)$$

$$\overline{\nabla T_{int}} = \frac{\int_v \nabla T\phi(1-\phi)dv}{\int_v \phi(1-\phi)dv} \quad (16)$$

297 where  $\phi(1-\phi)$  allows capturing only the interface region between the two phases.  
 298 Figure 7 shows the temperature gradient in and around the drop at a given time  
 299 for our reference simulation. Most heat transfer between the metal drop and the  
 300 magma ocean occurs at the drop front side, while the back half only accounts for  
 301 about 15% of the total. The existence of a hot thermal wake and the external  
 302 recirculation behind the drop that encapsulates and entrains magma with the  
 303 sinking drop are the main reasons limiting back thermal exchanges (41; 27).  
 304

305 A close view of the temperature field and of the thermal boundary layer  
 306 is shown in Figure 8. We define the thermal boundary layer thickness as the  
 307 distance from the drop interface to a point where the temperature anomaly  
 308 reaches 1% of its interfacial value. The boundary layer is very thin at the drop

309 front section, where most thermal exchanges are carried out. It significantly  
 310 increases behind the drop. An example of thickness measurement is shown in  
 311 Figure 8 (Right) at the thinnest position, i.e. at the front of the drop. In order  
 312 to give a global estimate around the drop, we also define the average boundary  
 313 layer thickness as

$$\delta_{T_{av}} = \frac{\overline{T_{int}} - T_m}{\nabla T_{int}}. \quad (17)$$

#### 314 4. Parametric study and scaling analysis

315 We now present our systematic exploration of the parameter space, changing  
 316 the magma ocean viscosity or the drop initial radius as shown in Table 2, from  
 317 our reference simulation #4. We then analyse our results in terms of scaling  
 318 laws. In particular we determine the influence of the Peclet number on the  
 319 dimensionless parameters defined in the previous section: the time and length  
 320 of equilibration, the normalized thermal boundary layer thickness, the Nusselt  
 321 number, and the dimensionless magma ocean volume affected by thermal ex-  
 322 changes.

##### 323 4.1. Time and length of equilibration

324 As expected from previous studies of drop dynamics, but largely neglected  
 325 in geophysical applications (see e.g. discussions in 7; 27), the characteristic  
 326 time and length of equilibrium depend on the viscosity contrast between the  
 327 metal drop and the magma ocean. As presented in Figure 9, increasing the  
 328 viscosity ratio increases the required time for thermal equilibration (Figure 9  
 329 Left), mostly because a larger ambient viscosity limits advective heat exchanges.  
 330 We can observe in this Figure 9 (Left) two different power laws depending on  
 331 the dynamic regime of the drop. In the first regime (non-deformable drop,  
 332  $R_\mu > 1000$ ), the equilibration characteristic time is highly dependent on the  
 333 viscosity ratio, whereas in the second regime (deformable drop,  $R_\mu < 200$ ),

334 the equilibration characteristic time depends slightly on the viscosity ratio and  
 335 highly on the deformation of the drop. The evolution of the equilibration length  
 336 is non-monotonic (Figure 9 Right), because the magma ocean viscosity also  
 337 influences the falling velocity. Globally, with a more viscous ambient fluid, the  
 338 thermal equilibrium between the two phases occurs less deeply in the magma  
 339 ocean, as we predicted in our previous work (27).

340 The drop size at a given viscosity ratio also influences the thermo-chemical  
 341 equilibration (see 20, for a fixed spherical shape). Increasing the initial radius of  
 342 the liquid metal drop decreases the surface of exchange over volume initial ratio,  
 343 and increases the drop falling velocity: we thus expect an increase of both the  
 344 characteristic time and length, as confirmed in Figure 10. In (27), we predicted  
 345 that increasing the drop initial radius also leads to surface extension due to  
 346 drop distortion, hence to faster equilibration compared to a purely spherical  
 347 drop: this effect is however limited, because drop deformation mostly occurs at  
 348 the back of the drop, while heat exchanges takes place mostly at the front.

349 Those two series of results can be rationalized by considering dimensionless  
 350 properties as a function of the Peclet number. Here, we normalize the equilib-  
 351 rium time by the thermal diffusion time and the equilibrium length by the initial  
 352 drop radius. Results are shown in Figure 11. The thermal equilibrium time for  
 353 a high Peclet, spherical drop theoretically scales as  $Pe^{-0.5}$  (see e.g. 30). Here  
 354 we find

$$t_c^* = 2.45Pe^{-0.59 \pm 0.01}. \quad (18)$$

355 This acceleration of the equilibration time compared to the theoretical model  
 356 may be a signature of the drop deformation at large Peclet. Correspondingly,  
 357 the length needed to reach the equilibration increases monotonically with Peclet  
 358 number following

$$l_c^* = 2.37Pe^{0.41 \pm 0.01}, \quad (19)$$

359 in agreement with a quasi-constant falling velocity, i.e.  $l_c = V \times t_c$ . In conclu-  
 360 sion, when the flow advection measured by the Peclet number increases, thermal  
 361 equilibration occurs faster but deeper in the magma ocean, which is of impor-  
 362 tance for Earth’s building models (31).

363 *4.2. Heat exchanges*

364 Simply equilibrating large-scale heat advection along the drop surface by  
 365 with heat diffusion through the thermal boundary layer perpendicular to it, the  
 366 theoretical size of the thermal boundary layer normalised by the drop radius  
 367 classically scales as  $Pe^{-0.5}$ : this was verified numerically by (20) for a rigid  
 368 falling sphere. As shown in Figure 12 (Left), we also recover this scaling at the  
 369 drop front, where most heat exchange occurs: the best fit gives

$$\delta_T^* = 2.53Pe^{-0.5}. \quad (20)$$

370 With the deformable drops considered here however, the boundary layer thick-  
 371 ness strongly varies around the metal drop: we thus compute a characteristic  
 372 average value  $\delta_{T_{av}}$  from Eq. 17, normalised by the initial radius. Results are  
 373 shown in Figure 12 (Right), with the best fit scaling law

$$\delta_{T_{av}}^* = 10.7Pe^{-0.6 \pm 0.01}. \quad (21)$$

374 Over the explored range, the average thickness is at least three times larger  
 375 than the front one. The larger-than-expected 0.6 exponent might again be a  
 376 signature of drop distortion at large Peclet number.

377 Then by definition, the Nusselt number averaged over the drop surface should  
 378 scale as  $1/\delta_{T_{av}}^*$ . This is indeed recovered, as shown in Figure 13 with the best  
 379 fit scaling law

$$Nu = 0.08Pe^{0.63 \pm 0.02}. \quad (22)$$

380 Note that  $Nu$  varies over time in many cases in this study: we consider here its  
 381 time-mean averaged value.

382 Comparing this result with the one obtained in the previous section, we also  
 383 recover that the typical dimensionless time for equilibration  $t_c^*$  scales like  $1/Nu$ ,  
 384 as expected. This proves the self-consistency of our measurements.

### 385 4.3. Volume of heated magma ocean

386 In the wake of the drop, the magma ocean is thermally affected by its passage.  
 387 Because of heat diffusion within the magma ocean, the affected volume widens  
 388 with time. But on the short times, at a given depth of the drop  $z$ , it can  
 389 be estimated by simply balancing the heat that has passed through the drop  
 390 interface with the heat accumulated in this volume of magma ocean, whose  
 391 temperature has increased by a given amount larger or equal to  $T_C$ . We then  
 392 predict

$$V_{o^*} = \frac{\text{Volume of heated magma}}{\text{Initial drop volume}} \sim 3 \frac{Nu}{Pe} \frac{z}{R} \frac{\Delta T_0}{T_C}. \quad (23)$$

393 with  $\Delta T_0$  the initial temperature difference between the two phases. Results  
 394 in Figure 14 show a good agreement with a small relative error for various  
 395 depths  $z = 10, 20, 30R$  and temperature contrast  $T_C = 1K$ , using the previously  
 396 determined scaling for  $Nu$ . This indicates the self-coherence of our numerical  
 397 results from a fluid dynamics point of view through the energy conservation.  
 398 ~~With this scaling law, we conclude that the mixing in the magma ocean induced~~  
 399 ~~by the passage of each drop is very small.~~ Note that here the falling drop  
 400 encapsulates in its wake a small volume of silicate while the reminder of the  
 401 ambient fluid remains largely motionless or laminar. However, the thermal  
 402 contamination in the magma ocean induced by the passage of each drop is very  
 403 small. This volume will always eventually decrease due to thermal diffusion and  
 404 will always go to zero in a long term due to the absence of viscous dissipation in

405 this study. In the context of planetary core formation, the viscous dissipation  
 406 effect is very important for the release of gravitational potential energy due  
 407 only to the fall of the drop. Thus, long after the drop has equilibrated with  
 408 the magma ocean, it still produces a thermal wake as its gravitational potential  
 409 energy. Thus, in the segregation of the drops, the phenomenon of diffusion of  
 410 the affected volume of the magma ocean does not always tend towards zero.  
 411 In addition, the analytical law proposed by the energy balance between the  
 412 drop and the magma ocean in Eq. 23, is of interest for planet building models  
 413 by passing from the one drop scenario to a cloud of drops of different sizes  
 414 resulting from an impactor core with a radius of 10-100 km. Thus, the volume  
 415 of the total amount of heat exchanged between this cloud and the magma ocean,  
 416 plays an important role on the global heat budget. Our conclusion should be re-  
 417 evaluated in the presence of global magma motions, coming e.g. from turbulent  
 418 convection, depending on the typical excited time- and length-scales. But this  
 419 is beyond the scope of the present paper.

## 420 **5. Influence of a temperature dependent viscosity**

421 The magma ocean viscosity increases from the surface to the base of the  
 422 magma ocean because of the combined effects of temperature and pressure (21).  
 423 Those large-scale variations are irrelevant in the context of our local study;  
 424 nevertheless, during the drop fall over the typical length of  $\sim 200R$  considered  
 425 here, the temperature of the liquid magma ocean increases because of heat  
 426 exchanges with the drop, therefore its viscosity decreases at a given pressure  
 427 (i.e. depth) following the equation of (21) for anhydrous liquid

$$\mu_T = 0.00033e^{(6400/(T-1000))} Pa.s. \quad (24)$$

428 Here, we investigate the influence of such a temperature dependent viscosity

429 on the dynamics, stability and thermal evolution of a drop. For a given initial  
430 viscosity ratio, the initial magma ocean temperature is computed using (24),  
431 and we then consider an initial temperature difference with the hot metal drop  
432 of  $\Delta T = 100$  K or  $\Delta T = 1000$  K. We focus on 3 reference cases, only changing  
433 the viscosity ratio (see Table 2). Those cases are first presented in the absence  
434 of temperature dependent viscosity:

- 435 • The non-deformable drop case (simulation #3 in Table 2,  $Re=0.76$  and  
436  $Pe=254$ ) is presented in Figure 15. Drop's shape remains mostly constant.  
437 The temperature is close to uniform inside the drop because of internal  
438 recirculation, and progressively decreases in the wake. Most heat transfer  
439 takes place in the front.
- 440 • The weakly deformable drop case (simulation #5 in Table 2,  $Re=21.8$  and  
441  $Pe=728.36$ ) is presented in Figure 16. The drop quickly deforms towards  
442 a spherical cap, associated with a strong release of heat in its wake. The  
443 system then reaches a quasi-steady state, with the most surprising feature  
444 being a more rapid temperature decrease in the drop than in the wake,  
445 leading to a positive heat transfer from the silicate to the iron in the drop's  
446 back. Nevertheless, most heat transfer still takes place at the front.
- 447 • Finally, the strongly deformable drop case (simulation #6 in Table 2,  
448  $Re=47.6$  and  $Pe=793.73$ ) is presented in Figure 17. Here, the drop shape  
449 keeps oscillating over the whole depth because of competing surface ten-  
450 sion and inertial forces. This induces oscillatory temperature changes in  
451 the wake, associated to periodic thermal plumes emitted from the drop  
452 sides, and strong inhomogeneous fluxes within the magma ocean. Nev-  
453 ertheless heat transfers between iron and silicate are still largely focused  
454 at the drop's front, explaining while this case is not associated with any  
455 specific signature in the previous section.

456 We now re-run those three cases using the previously defined temperature-  
457 dependent viscosity.

### 458 *5.1. Drop dynamics*

459 Figure 18 shows the normalized average velocity of each drop as a function  
460 of the normalized time for constant magma ocean viscosity in black lines and  
461 for temperature dependent viscosity with  $\Delta T = 100$  K ( $\Delta T = 1000$  K) in red  
462 (blue) dashed lines. The normalized average velocity for the non-deformable  
463 drop (Figure 18 Left) with  $\Delta T = 100$  K, increases moderately by about 4.8%  
464 compared to the constant viscosity case, keeping the spherical shape without  
465 change in the morphology. For  $\Delta T = 1000$  K, the drop deforms from the  
466 back side and its velocity strongly increases by about 26%; concomitantly, the  
467 average viscosity around the drop decreases by 93%, explaining this significant  
468 dynamical change. On the contrary, for the weakly deformable drop (Figure  
469 18 Middle) and the strongly deformable drop (Figure 18 Right), no significant  
470 dynamical change is observed, despite a large viscosity decrease in the associated  
471 thermal boundary layer (by 76% and 92%, respectively, for  $\Delta T = 1000$  K; see  
472 also Figure 19). This indicates that the drop dynamics is already mostly inviscid  
473 in the absence of temperature-dependent viscosity, as can be guessed from the  
474 corresponding values of the Reynolds number (see caption of Figures 16 and  
475 17).

### 476 *5.2. Drop fragmentation*

477 In the most extreme previous case (the strongly deformable drop with  $\Delta T =$   
478 1000 K), Figure 19 indicates that the hot silicate layer surrounding the drop has  
479 a viscosity value of the order 0.05 Pa.s: assuming such a viscosity uniformly in  
480 the ambient magma ocean, our previous study (27) predicts a rapid fragmenta-  
481 tion, which is not observed here. Actually the viscosity contrast at the interface

482 does not influence the drop stability, because the thermal boundary layer where  
 483 the low viscosity is localised is very thin in front of the drop, compared to any  
 484 relevant dynamical length scale; besides, the wake has no influence on the drop.  
 485 Temperature dependent viscosity only affects the drop’s dynamics and fragmen-  
 486 tation when flows and temperature change on comparable scales, in upfront or  
 487 sides locations.

488 To further prove this, we performed a simulation with a drop radius of 25  
 489 mm and a viscosity ratio of 200 for constant magma ocean viscosity first, then  
 490 for  $\Delta T = 1000$  K dependent magma ocean viscosity (simulation #10 in Ta-  
 491 ble 2). Figure 20 (Left) shows the Jellyfish fragmentation mode when constant  
 492 magma ocean viscosity is considered (more details can be found in 27) . The  
 493 normalized time ( $t_{bk}^* = \frac{t_{bk}V}{2R} \sqrt{\frac{\rho_d}{\rho_m}}$ ) and distance ( $d_{bk}^* = \frac{d_{bk}}{R}$ ) of breakup equal  
 494 to 3.8 and 10.7 respectively. For temperature-dependent viscosity (Figure 20  
 495 middle), another Jellyfish fragmentation mode is observed, with time and dis-  
 496 tance of breakup equal to 2.3 and 5.6 respectively. Actually, here, the extended  
 497 jellyfish membranes form filaments, where thermal effects are very important.  
 498 These membranes sink into a less viscous medium whose thickness is compara-  
 499 ble to the membranes thickness (see Figure 20 Right). ~~So, the inertia forces in~~  
 500 ~~this zone are stronger than the surface tension, and the fragmentation occurs.~~  
 501 Thus, the filaments move freely in this zone with low viscous constraint and  
 502 therefore separate from the drop volume leading to the fragmentation.

503 Note finally that the local dimensionless numbers, taken at the mean tem-  
 504 perature (and associated viscosity) of the thermal boundary layer, become  
 505  $Re = 1000$ ,  $We = 19$  and  $R_\mu = 10$ . From Figures 4, 12 and 13 of our pre-  
 506 vious study (27), we find consistent results for the fragmentation mode of the  
 507 drop, as well as for its time and distance of breakup, accounting for these di-  
 508 mensionless numbers (To compare with our previous study,  $Re$  and  $We$  should

509 be multiplied in this study by a factor of 2 because in (27),  $Re$  and  $We$  are  
510 calculated by the drop diameter).

511 Hence, temperature dependent magma ocean viscosity influences the drop  
512 fragmentation in the filament forming regimes only. In such regimes, the results  
513 in (27) as a function of  $Re$ ,  $We$  and  $R_\mu$  already allow predicting fragmentation  
514 mode, breaking time and distance by considering local values of the dimension-  
515 less numbers.

### 516 5.3. Thermal evolution

517 In Figure 21, we compare the normalized mean iron temperature for each  
518 case as a function of normalized time. For a non-deformable drop (Figure  
519 21 Left), the average temperature for  $\Delta T = 100$  K (red dashed lines) and  
520  $\Delta T = 1000$  K (blue dashed lines) temperature-dependent viscosity decreases  
521 by about 6.1% and 20.8% with respect to the constant viscosity case (black  
522 line). As a consequence, it significantly changes the characteristic time and  
523 length of equilibration (see Table 3). For a weakly deformable drop (Figure  
524 21 Middle), the average temperature evolution with  $\Delta T = 1000$  K changes  
525 only by about 13.6%; no difference is measured for a strongly deformable drop  
526 (Figure 21 Right). As for the fall velocity, temperature dependent viscosity  
527 influences significantly the thermal evolution of non-deformable drops only (i.e.  
528 the drops in the Stokes regime). Note finally that in the intermediate regime, the  
529 characteristics time and length of equilibration decrease slightly with a temper-  
530 ature dependent viscosity compared to constant magma ocean viscosity case,  
531 whereas in the Stokes regime, the equilibrium characteristic length increases  
532 with a temperature dependent viscosity, in contrast to the characteristic time  
533 of equilibration (see Table 3).

534 As for the volume of heated magma ocean shown in Figure 22, no significant  
535 change is observed in the heated volume for all cases with  $\Delta T = 100$  K (red

536 dashed lines). The volume of heated magma ocean increases by about 1.5 to  
537 2 times compared to the constant viscosity case (black line) for  $\Delta T = 1000$  K  
538 (blue dashed lines) due to the initial larger temperature difference; but the  
539 curves remain parallel, hence exhibiting no specific dynamical signature.

Table 3: The change in characteristics time and length for cases of temperature-dependent viscosity.

<i>Simulation</i>	$\Delta T$	$t_c^*$	$l_c^*$
#3 (constant magma ocean viscosity)	100	0.1	24.25
#3a ( $T$ dependent $\mu_m$ )	100	0.0975	25.6
#3b ( $T$ dependent $\mu_m$ )	1000	0.082	27
#5 (constant magma ocean viscosity)	100	0.05	35.14
#5a ( $T$ dependent $\mu_m$ )	100	0.0496	33.33
#5b ( $T$ dependent $\mu_m$ )	1000	0.045	31.25
#6 (constant magma ocean viscosity)	100	0.045	32
#6a ( $T$ dependent $\mu_m$ )	100	0.044	29.4
#6b ( $T$ dependent $\mu_m$ )	1000	0.042	27.7

540 Finally, we calculate the heat transfer between the two phases "Nusselt num-  
541 ber" of all drops in this section for a temperature dependent viscosity. Then, we  
542 compare these results with the correlations proposed in the experimental and nu-  
543 merical studies of the penetration of a hot diapir through a highly temperature-  
544 dependent viscous medium (42; 43). These correlations of the Nusselt number  
545 are done for non-deformable spherical drops of low Reynolds number and are  
546 given as follows:

$$Nu = 1 + C_1 Pe^{1/3} \quad (25)$$

547 where  $C_1 = 0.45 \pm 0.09$ .

$$Nu = 0.795 + 0.459 [Pe \left( \frac{\Delta T}{\ln 10} \right)^3 \frac{\overline{\mu_{int}}}{\mu_m}]^{-1/5}]^{1/2} \quad (26)$$

548 The Eq. 25 has been proposed experimentally by (42) and the Eq. 26 has been  
549 proposed numerically by (43). The comparison of the Nusselt numbers between

our numerical results and the Eqs. 22, 25 and 26 is shown in Table 4.

Table 4: The comparison of the Nusselt numbers for cases of temperature-dependent viscosity between our numerical results and the Eqs. 22, 25 and 26.

<i>Simulation</i>	<i>Nu: this study</i>	<i>Nu: Eq. 22</i>	<i>Nu: Eq. 25</i>	<i>Nu: Eq. 26</i>
#3a	2.65	2.72	$3.91 \pm 0.58$	3.36
#3b	2.95	3.07	$4.10 \pm 0.62$	2.82
#5a	5.15	5.17	$5.08 \pm 0.82$	4.93
#5b	5.21	5.33	$5.15 \pm 0.83$	3.65
#6a	5.28	5.36	$5.16 \pm 0.83$	5.06
#6b	5.35	5.36	$5.16 \pm 0.83$	4.58

550

551 We observe that our numerical results are consistent with Eq. 26 for the  
 552 non-deformable drops and with Eq. 25 for the deformable drops. This proves  
 553 the validity of our calculations in this section. We further note that our Nus-  
 554 selt number scaling law in section 4.2 (Eq. 22) is valid for this section of a  
 555 temperature-dependent viscosity.

## 556 6. Conclusions and future work

557 We have carried out series of numerical simulations to characterize the ther-  
 558 mal exchanges between a falling drop and a viscous ambient fluid, exploring a  
 559 new parameter range relevant for the geophysical application of a hot liquid iron  
 560 drop falling in a magma ocean. We have shown that because of drop distortions,  
 561 thermal equilibration properties slightly change from the theoretical predictions  
 562 based on diffusive heat exchanges through a laminar thermal boundary layer.  
 563 We have also tested that accounting for a temperature-dependent viscosity in the  
 564 magma ocean barely influences the obtained results, except for limited cases like  
 565 non-deformable, low Reynolds number drops or Jellyfish fragmentation mode.  
 566 Our most relevant results for geophysical application are the scaling laws for the  
 567 normalized length of equilibration and for the Nusselt number, which both in-  
 568 crease monotonically with the Peclet number as  $Pe^{0.41}$  and  $Pe^{0.63}$ , respectively.

569 Future work should now consider (i) the presence of convection in the ambi-  
570 ent magma ocean, which could affect our conclusions providing the associated  
571 velocity at the drop scale is at least of similar order as the falling drop velocity,  
572 hence requiring extremely turbulent regimes; and (ii) chemical exchanges be-  
573 tween iron and silicates, which will determine the initial chemical state of the  
574 considered planet (see e.g. 44). Chemical and thermal constitutive equations  
575 being similar, similar equilibration scaling laws and dynamics are nevertheless  
576 expected.

577 **Acknowledgements**

578       The authors acknowledge funding by the ERC under the European Union's  
579 Horizon 2020 research and innovation program through Grant No. 681835-  
580 FLUDYCO-ERC-2015-CoG. This research also received funding from the French  
581 PNP program (INSU-CNRS), the French Government Laboratory of Excellence  
582 initiative No. ANR-10-LABX-0006, and the Région Auvergne. This paper is  
583 Laboratory of Excellence ClerVolc contribution no. XX. We are grateful to the  
584 Mésocentre Clermont Auvergne University for providing help as well as com-  
585 puting and storage resources.

586 **References**

- 587 [1] T. Kleine, C. Münker, K. Mezger, and H. Palme. Rapid accretion and  
588 early core formation on asteroids and the terrestrial planets from Hf-W  
589 chronometry. Nature, 418:952–955, 2002.
- 590 [2] M. Touboul, T. Kleine, B. Bourdon, H. Palme, and R. Wieler. Late forma-  
591 tion and prolonged differentiation of the Moon inferred from W isotopes in  
592 lunar metals. Nature, 450:1206–1209, 2007.
- 593 [3] D. J. Stevenson. fluid dynamics of core formation. Origin of the Earth,  
594 pages 231–249, 1990.
- 595 [4] R. Deguen, P. Olson, and P. Cardin. Experiments on turbulent metal-  
596 silicate mixing in a magma ocean. Earth Planet. Sci. Lett., 310:303–313,  
597 2011.
- 598 [5] R. Deguen, M. Landeau, and P. Olson. Turbulent metal - silicate mixing,  
599 fragmentation, and equilibration in magma oceans. Earth Planet. Sci. Lett.,  
600 391:274–287, 2014.
- 601 [6] M. Landeau, R. Deguen, and P. Olson. Experiments on the fragmentation  
602 of a buoyant liquid volume in another liquid. Fluid Mech., 749:478518,  
603 2014.
- 604 [7] J. B. Wacheul, M. LeBars, J. Monteux, and J. M. Aurnou. Laboratory  
605 experiments on the breakup of liquid metal diapirs. Earth Planet. Sci.  
606 Lett., 403:236245, 2014.
- 607 [8] J. B. Wacheul and M. Le Bars. Experiments on fragmentation and thermo-  
608 chemical exchanges during planetary core formation. Phys. Earth Planet.  
609 Int., 276:134 144, 2018.

- 610 [9] W. K. Hartmann and D. R. Davis. Satellite-sized planetesimals and lunar  
611 origin. Icarus, 24:504514, 1975.
- 612 [10] W. B. Tonks and H.J. Melosh. Core formation by giant impacts. ICARUS,  
613 100:326–346, 1992.
- 614 [11] J. Monteux, N. Coltice, F. Dubuffet, and Y. Ricard. Thermo-mechanical  
615 adjustment after impacts during planetary growth. Geophys. Res. Lett.,  
616 34:24201–24205, 2007.
- 617 [12] M. J. Walter and R. G. Tronnes. Early earth differentiation. Earth Planet.  
618 Sci. Lett., 225:253–269, 2004.
- 619 [13] J. Monteux, Y. Ricard, N. Coltice, F. Dubuffet, and M. Ulvrova. A model of  
620 metal-silicate separation on growing planets. Earth and Planetary Science  
621 Letters, 287:353–362, October 2009.
- 622 [14] J. D. Kendall and H. Melosh. Differentiated planetesimal impacts in a  
623 terrestrial magma ocean: fate of the iron core. Earth Planet. Sci. Lett.,  
624 448:2433, 2016.
- 625 [15] H. Genda, R. Brasser, and S.J. Mojzsis. The terrestrial late veneer from  
626 core disruption of a lunar-sized impactor. Earth and Planetary Science  
627 Letters, 480:2532, 2017.
- 628 [16] D. C. Rubie, H. J. Melosh, J. E. Reid, C. Liebske, and K. Righter. Mecha-  
629 nisms of metal-silicate equilibration in the terrestrial magma ocean. Earth  
630 and Planet. Sci. Lett., 205:239–255, January 2003.
- 631 [17] H. Ichikawa, S. Labrosse, and K. Kurita. Direct numerical simulation of an  
632 iron rain in the magma ocean. GEOPHYSICAL RESEARCH, 115:B01404,  
633 2010.

- 634 [18] H. Samuel. A re-evaluation of metal diapir breakup and equilibration in  
635 terrestrial magma oceans. Earth Planet. Sci. Lett., 313-314:105–114, 2012.
- 636 [19] T. W. Dahl and J. Stevenson. Turbulent mixing of metal and silicate during  
637 planet accretion and interpretation of the hf-w chronometer. Earth Planet.  
638 Sci. Lett., 295:177 – 186, 2010.
- 639 [20] M. Ulvrová, N. Coltice, Y. Ricard, S. Labrosse, and F. Dubuffet  
640 Velimský and M. Šrámek. Compositional and thermal equilibration of par-  
641 ticles, drops, and diapirs in geophysical flows. Geochem. Geophys. Geosyst.,  
642 12, 2011.
- 643 [21] B. B. Karki and L. P. Stixrude. Viscosity of mgsio<sub>3</sub> liquid at earth's mantle  
644 conditions : Implications for an early magma ocean. Science, 328:740–742,  
645 2010.
- 646 [22] T. Bonometti and J. Magnaudet. Transition from spherical cap to toroidal  
647 bubbles. Phys. Fluids, 18:052102, 2006.
- 648 [23] M. Ohta, Y. Akama, Y. Yoshida, and M. Sussman. Three-dimensional  
649 simulations of vortex ring formation from falling drops in an immiscible  
650 viscous liquid. Chem. Engng Japan, 42:648655, 2009.
- 651 [24] M. Ohta, S. Yamaguchi, Y. Yoshida, and M. Sussman. The sensitivity of  
652 drop motion due to the density and viscosity ratio. Phys. Fluids, 22:072102,  
653 2010.
- 654 [25] M. Ohta, Y. Akama, Y. Yoshida, and M. Sussman. Influence of the viscosity  
655 ratio on drop dynamics and breakup for a drop rising in an immiscible  
656 low-viscosity liquid. Fluid Mech., 752:383409, 2014.
- 657 [26] M. Ohta and M. Sussman. The buoyancy-driven motion of a single skirted

- 658 bubble or drop rising through a viscous liquid. Phys. Fluids, 24:112101,  
659 2012.
- 660 [27] B. Qaddah, J. Monteux, V. clesi, A.Bouhifd, and M. Le Bars. Dynamics  
661 and stability of an iron drop falling in a magma ocean. Phys. Earth Planet.  
662 Int., 289:75–89, 2019.
- 663 [28] X-Y. Luo, M-J. Ni, A. Ying, and M. Abdou. Application of the level set  
664 method for multi-phase flow computation in fusion engineering. Fusion  
665 Engineering and Design, 81:15211526, 2006.
- 666 [29] J. Hu, R. Jia, K.T. Wan, and X. Xiong. Simulation of droplet impingement  
667 on a solid surface by the level set method. COMSOL Conference in Boston,  
668 2014.
- 669 [30] V. Lherm and R. Deguen. Small-scale metal/silicate equilibration during  
670 core formation: The inuence of stretching enhanced diusion on mixing.  
671 Journal of Geophysical Research : Solid Earth, 123:10.49610.516, 2018.
- 672 [31] D.C. Rubie, F. Nimmo, and H.J Melosh. Formation of the earths core,  
673 treatise on geophysics evolution of the earth, second ed. Elsevier, 9:43–79,  
674 2015.
- 675 [32] A. M. Hofmeister. Mantle values of thermal conductivity and the geotherm  
676 from phonon lifetimes. SCIENCE, 283, 1999.
- 677 [33] C. W. Thomas and P.D. Asimow. Direct shock compression exper-  
678 iments on premolten forsteriteand progress toward a consistent high-  
679 pressure equationof state for cao-mgo-al2o3-sio2-feo liquids. JOURNAL  
680 OF GEOPHYSICAL RESEARCH: SOLID EARTH, 118:5738–5752, 2013.
- 681 [34] N. de Koker, G. Steinle-Neumann, and V. Vlček. Electrical resistivity and

- 682 thermal conductivity of liquid Fe alloys at high p and t, and heat flux in  
683 earth's core. PNAS, 109:4070–4073, 2012.
- 684 [35] H. Ichikawa, T. Tsuchiya, and Y. Tange. The p-v-t equation of state and  
685 thermodynamic properties of liquid iron. Journal of Geophysical Research:  
686 Solid Earth, 119:240–252, 2014.
- 687 [36] M. Pilch and C. A. Erdman. Use of breakup time data and velocity history  
688 data to predict the maximum size of stable fragments for acceleration-  
689 induced breakup of a liquid drop. Multiphase Flow, 13:741757, 1987.
- 690 [37] E. Villermaux and B. Bossa. Single - drop fragmentation determines size  
691 distribution of rain drops. Nat. Phys., 5:697702, 2009.
- 692 [38] S.S Jain, N. Tyagi, R. S. Prakash, R.V Ravikrishna, and G. Tomar. Sec-  
693 ondary breakup of drops at moderate weber numbers: Effect of density ratio  
694 and reynolds numbe. Int. J. Multiphase Flow, 117:2541, 2019.
- 695 [39] J. Crank. The mathematics of diffusion, 2nd edition. Clarendon Press,  
696 Oxford, 1975.
- 697 [40] R.C. Mittal and R.K. Jain. Redefined cubic b-splines collocation method  
698 for solving convection-diffusion equations. Applied Mathematical Modelling,  
699 36:5555 – 5573, 2012.
- 700 [41] J.R. Fleck, C.L. Rains, D.S. Weeraratne, C.T. Nguyen, D.M. Brand, S.M.  
701 Klein, J.M. McGehee, J.M. Rincon, C. Martinez, and P.L. Olson. Iron  
702 diapirs entrain silicates to the core and initiate thermochemical plumes.  
703 Nature Communications, 2018.
- 704 [42] N. M. Ribe. Diapirism in the earth's mantle: Experiments on the motion  
705 of a hot sphere in a fluid with temperature-dependent viscosity. Journal of  
706 Volcanology and Geothermal Research, 16(3):221 – 245, 1983.

- 707 [43] S. F. Daly and A. Raefsky. On the penetration of a hot diapir through  
708 a strongly temperature-dependent viscosity medium. Geophysical Journal  
709 International, 83:657681, 1985.
- 710 [44] M. Bouhifd and A. Jephcoat. The effect of pressure on partitioning of ni  
711 and co between silicate and iron-rich metal liquids: a diamond-anvil cell  
712 study. Earth Planet. Sci. Lett., 209:245255, 2003.

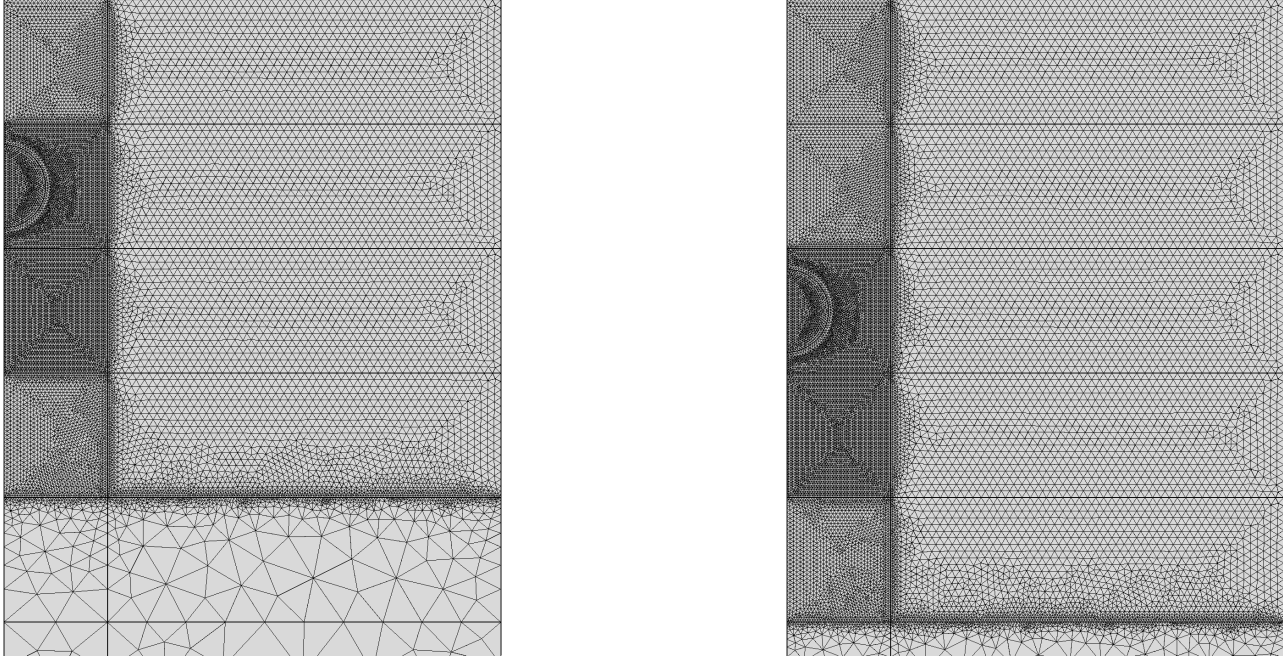


Figure 1: A zoom illustrating our adaptive mesh (left) and the method for mesh evolution over time when the drop reaches the bottom of the finest mesh region (right).

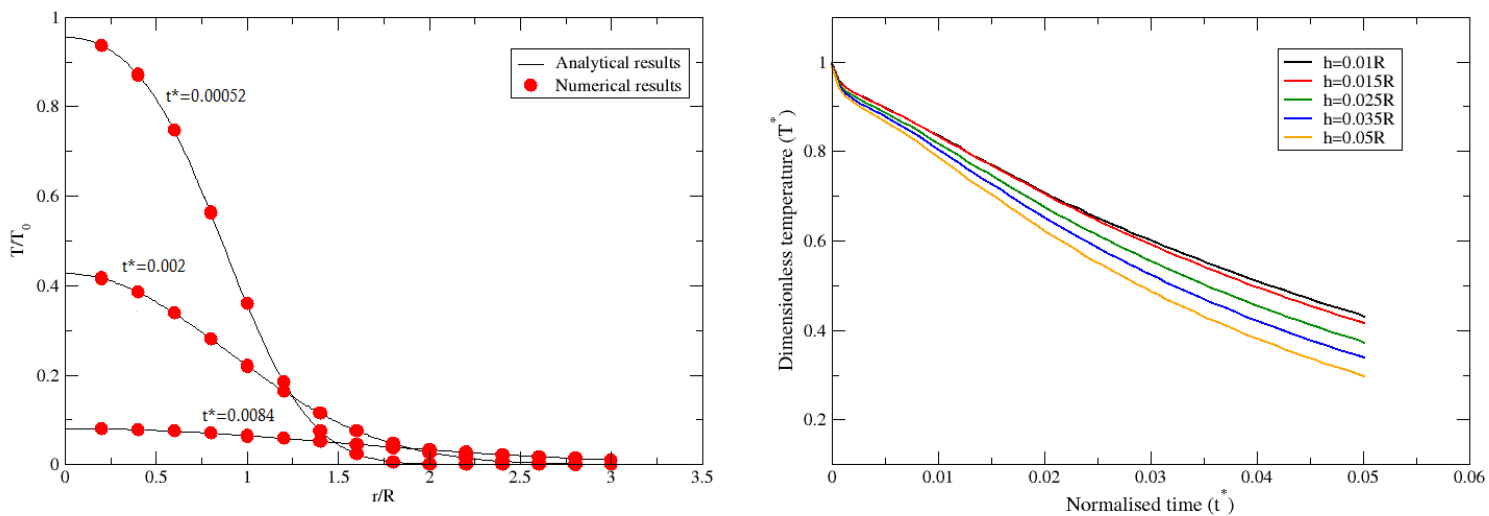


Figure 2: Left: comparison of our numerical results with the analytical results of (39) for the radial profile of the normalised temperature anomaly for a non-deformable and immobile drop. Right: comparison of the time evolution of the normalised mean temperature anomaly determined with different mesh sizes for a deformable and mobile drop (simulation #4 in Table 2).

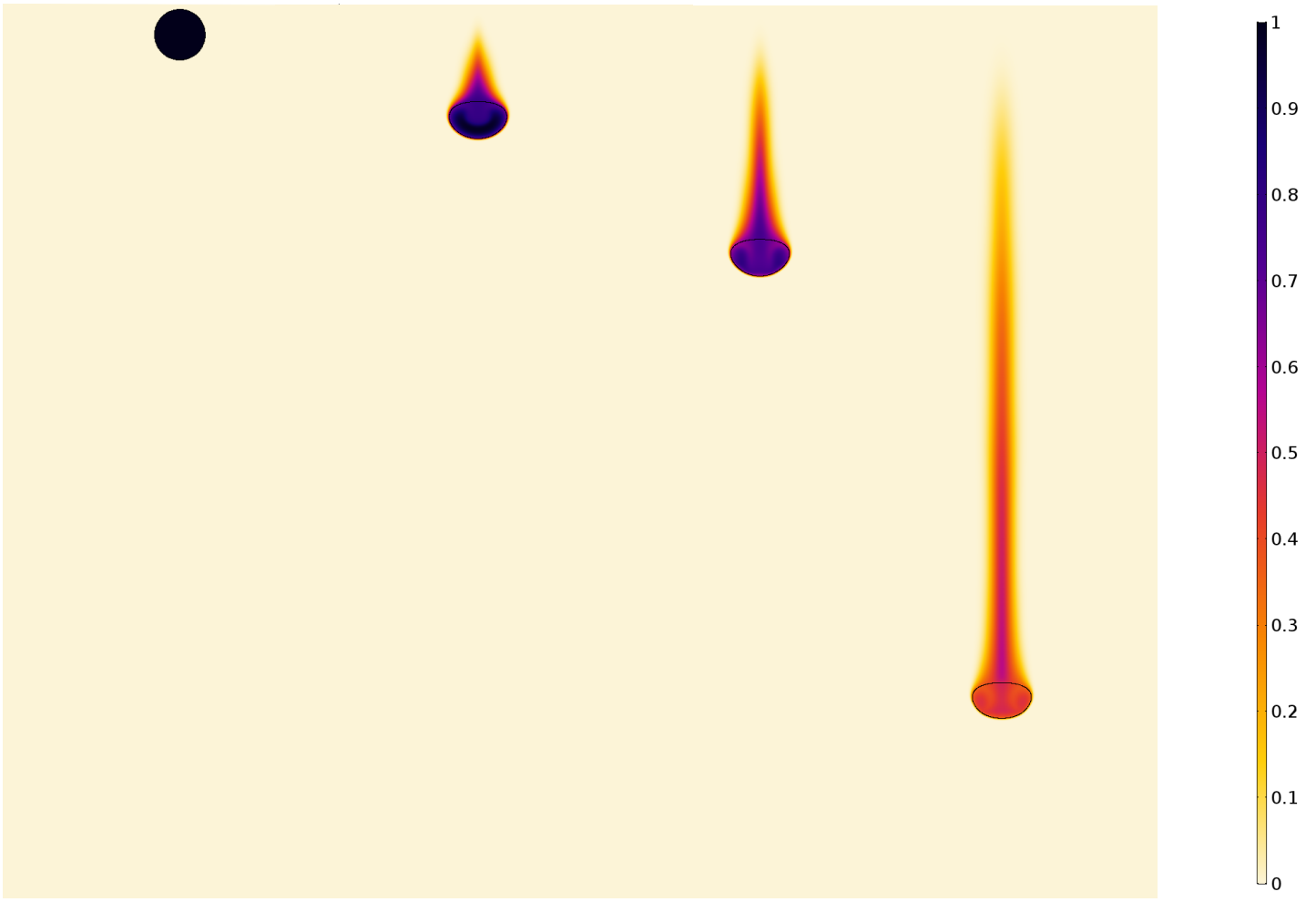


Figure 3: Dynamical and thermal evolutions of the metal drop as a function of time for simulation #4 in Table 2. The color presents the temperature anomaly normalised by its initial value  $T^*$ . The black solid line separates the metallic material from the magma ocean. From left to right, the time normalised by the thermal diffusion time is  $t^* = 0, 0.01, 0.02$  and  $0.05$ .

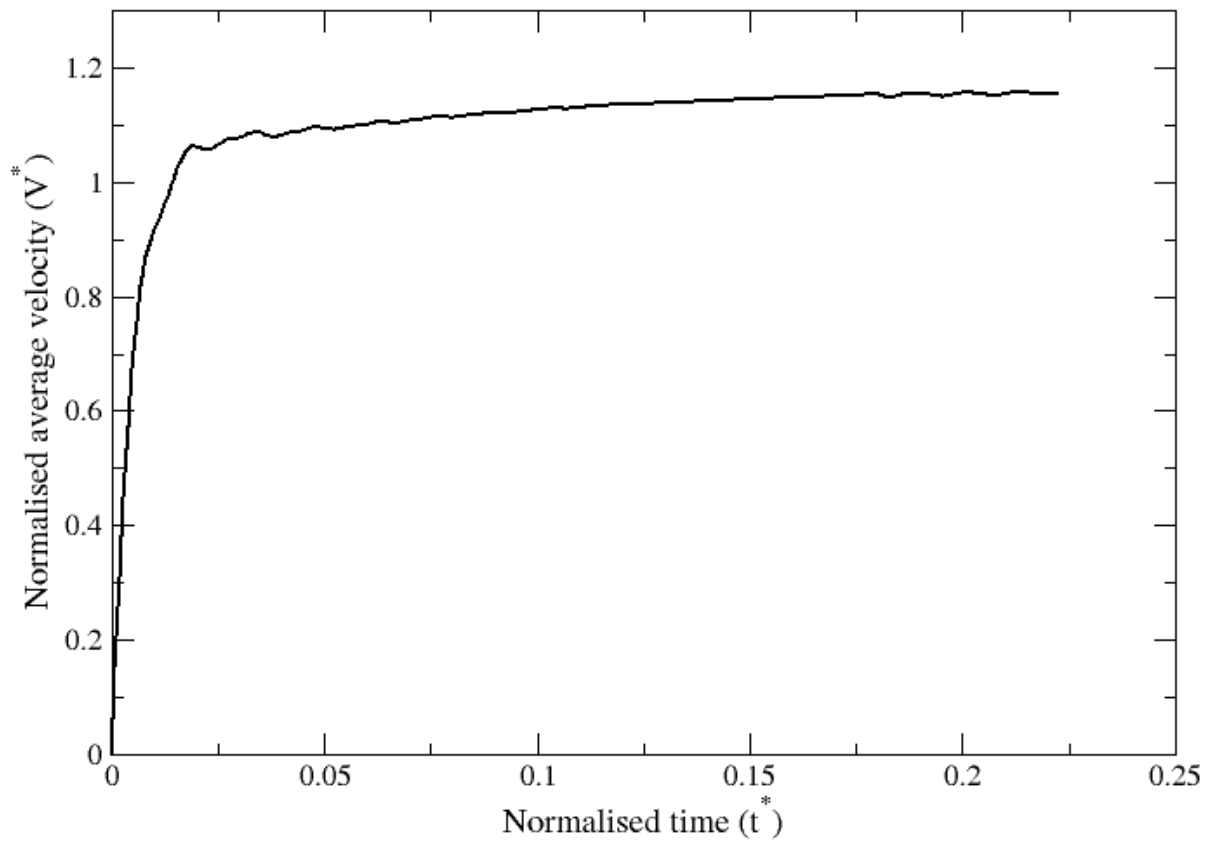


Figure 4: Normalized average velocity of the metal drop as a function of normalized time for simulation #4 in Table 2.

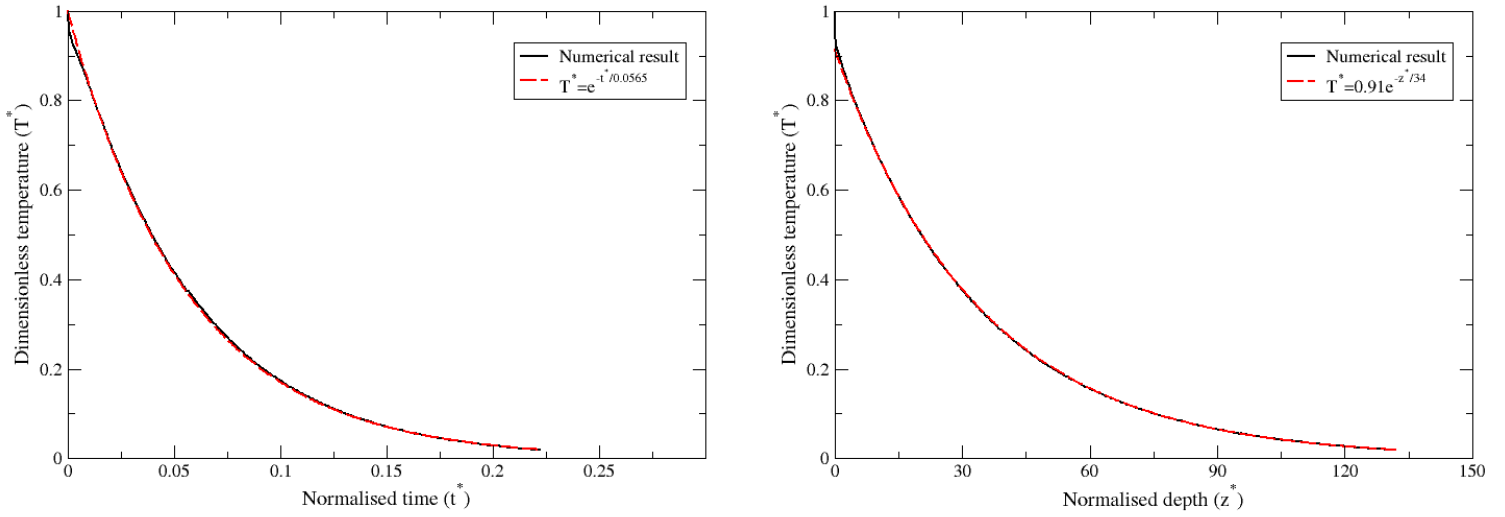


Figure 5: Normalized average temperature anomaly of the metal drop as a function of normalized time (left) and depth (right) for simulation #4 in Table 2. The black lines represent our numerical results and the red dashed lines represent the exponential fits from Eq. 13. The correlation coefficient for the two fits is 0.9999.

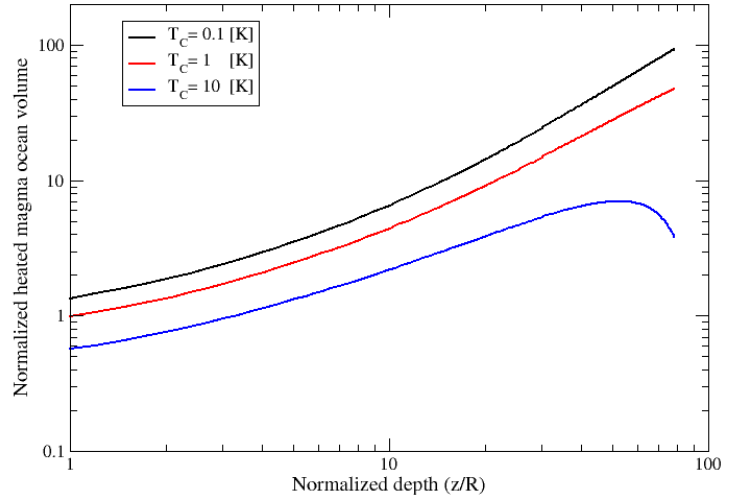


Figure 6: Left: volume of heated magma ocean ( $T_C = 1$  K) once the drop reaches a time  $t^* = 0.067$  and a depth  $z = 37R$  in our simulation #4 in Table 2. Right: normalized heated magma volume as a function of normalized depth for different values of  $T_C$ .

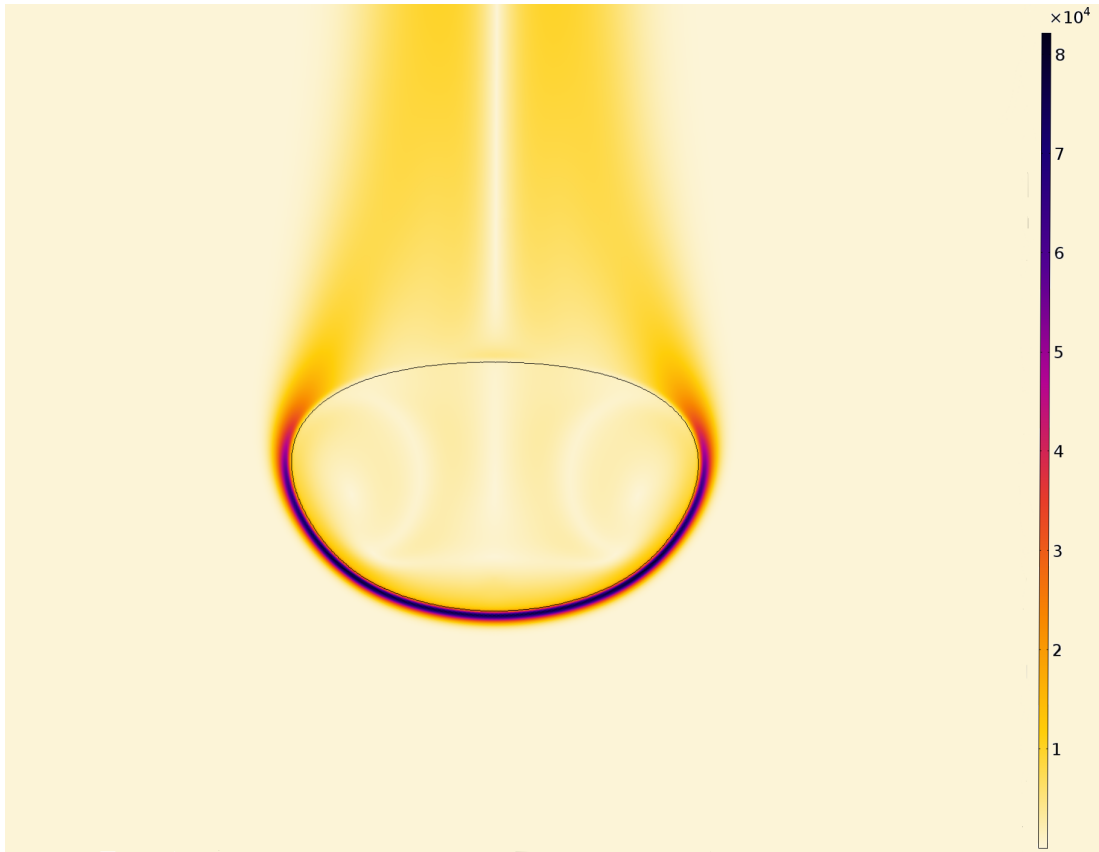


Figure 7: Temperature gradient ( $K/m$ ) in and around the drop for our reference simulation #4 in Table 2 at time  $t^* = 0.055$ .

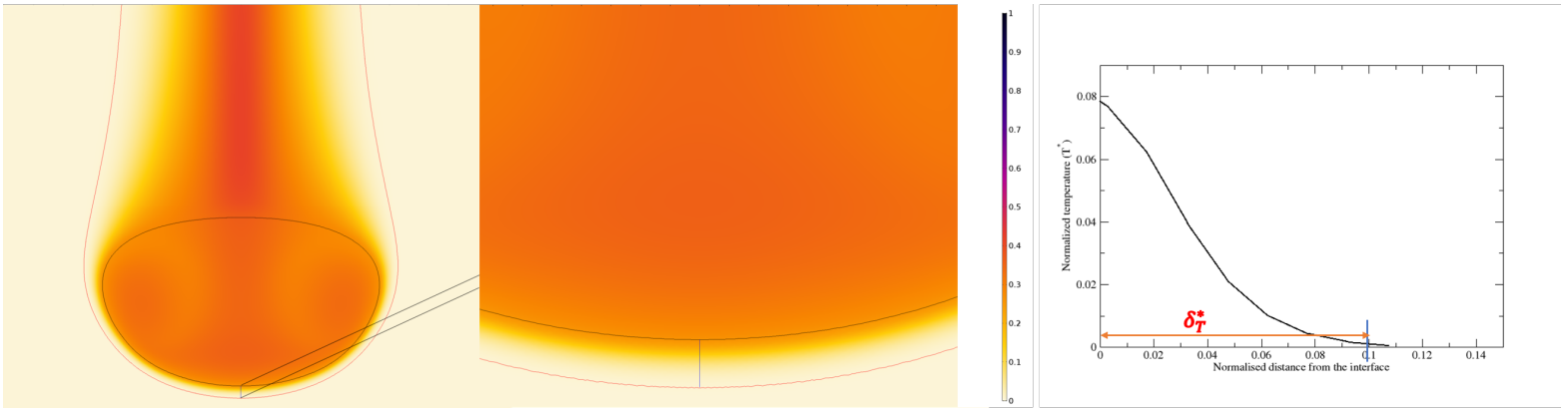


Figure 8: Left: temperature anomaly (colorscale) and contour of the thermal boundary layer (red line) around the drop (black line) for our reference simulation #4 in Table 2 at time  $t^* = 0.067$ . Middle: zoom at the drop front. Right: temperature profile of the thermal boundary layer in front of the drop and determination of the local boundary layer thickness.

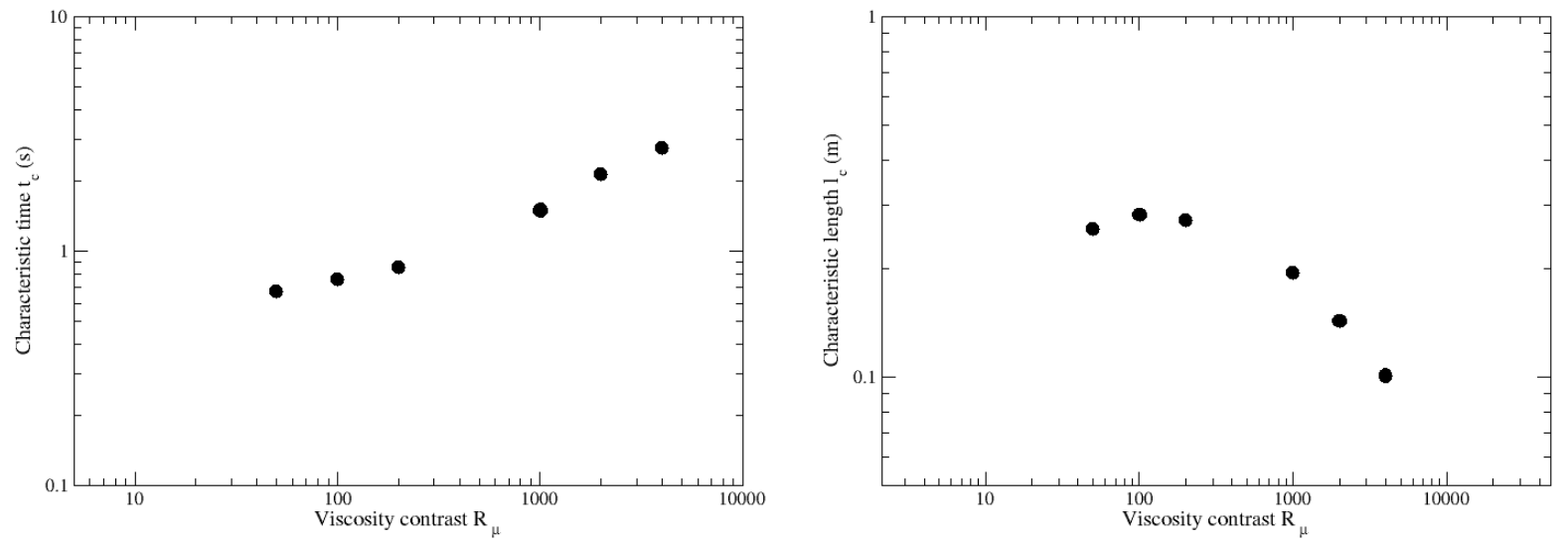


Figure 9: Characteristic time (Left) and length (Right) of equilibration as a function of the viscosity contrast (see Eq. (13)).

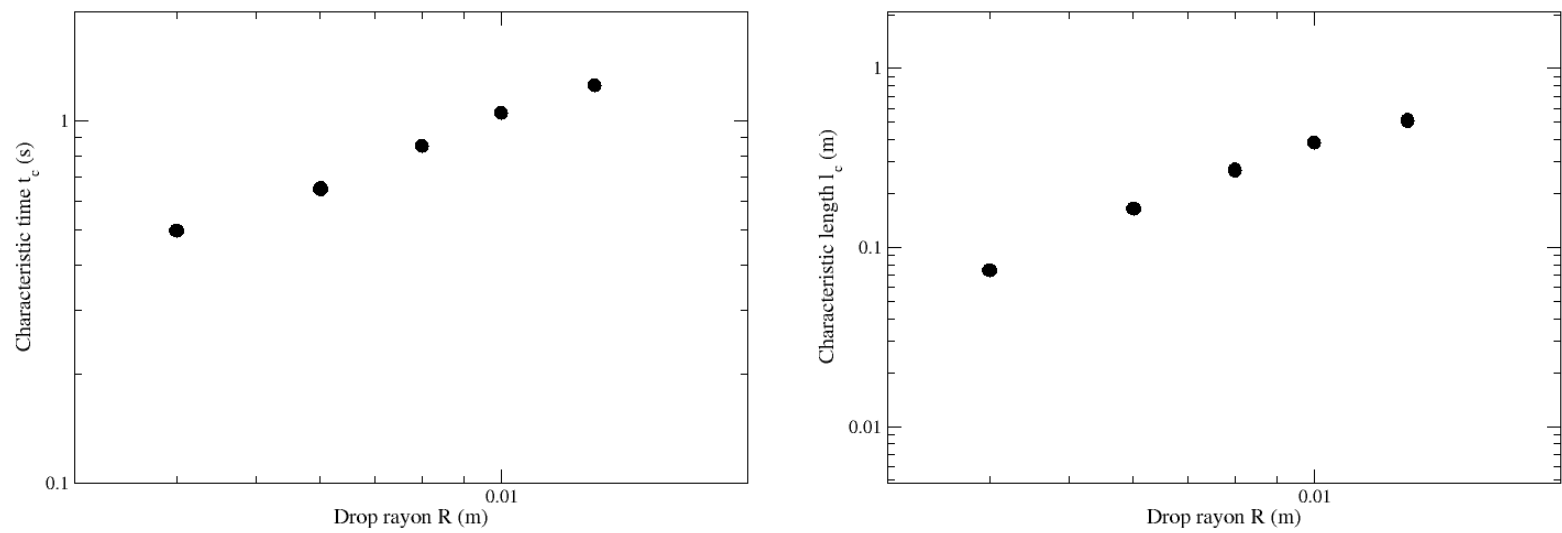


Figure 10: Characteristic time (Left) and length (Right) of equilibration as a function of the drop initial radius (see Eq. (13)).

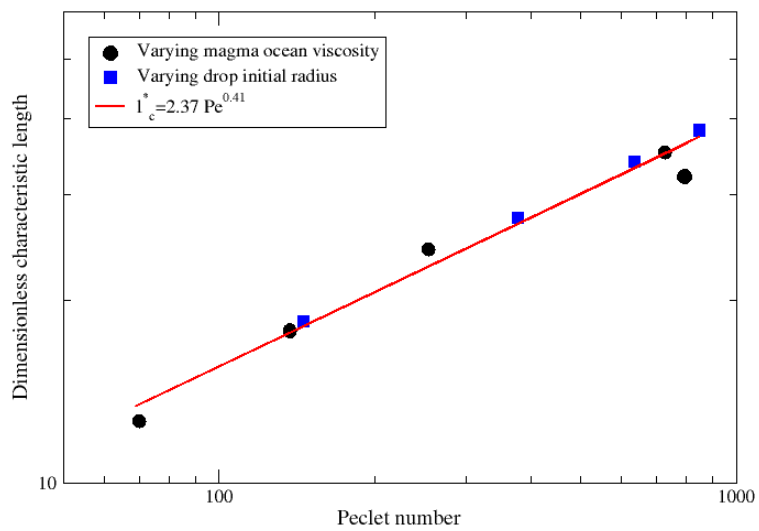
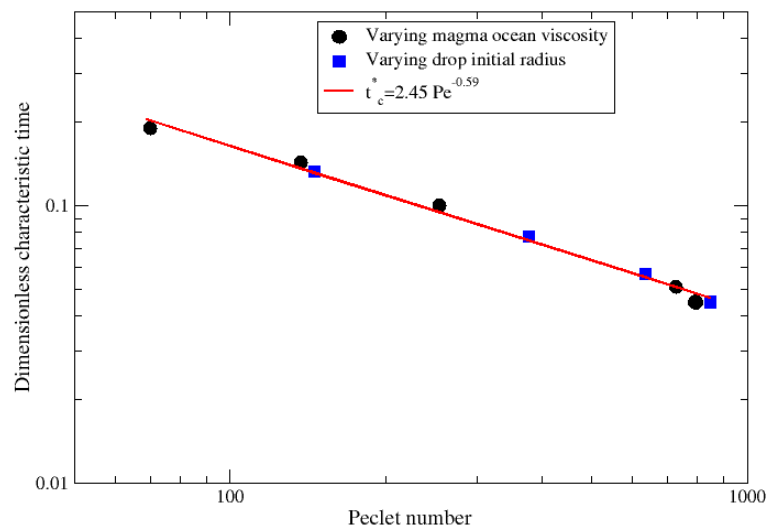


Figure 11: Dimensionless equilibrium time (Left) and length (Right) as a function of the Peclet number.

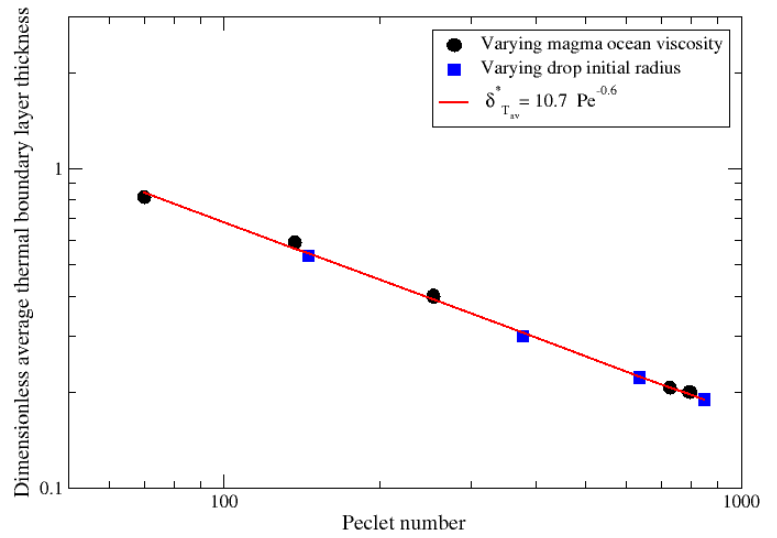
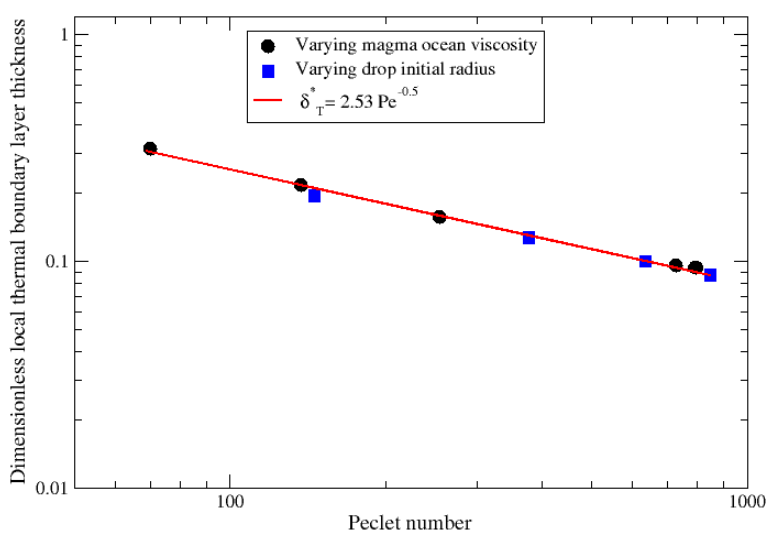


Figure 12: Dimensionless thickness of the thermal boundary layer at the drop front as a function of Peclet number (Left). Dimensionless average thickness of the thermal boundary layer around the drop as a function of Peclet number (Right).

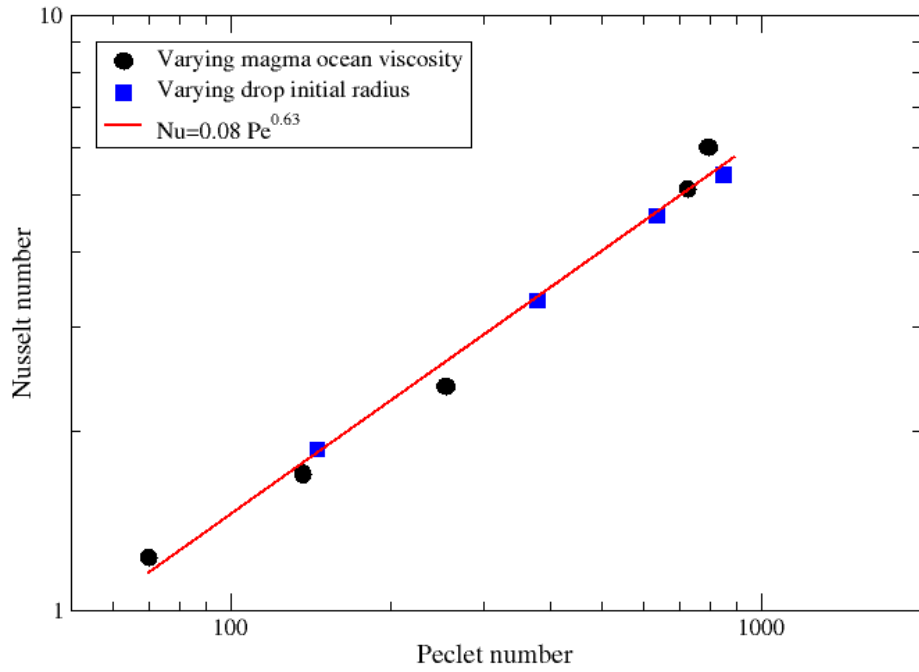


Figure 13: Nusselt number as a function of Peclet number

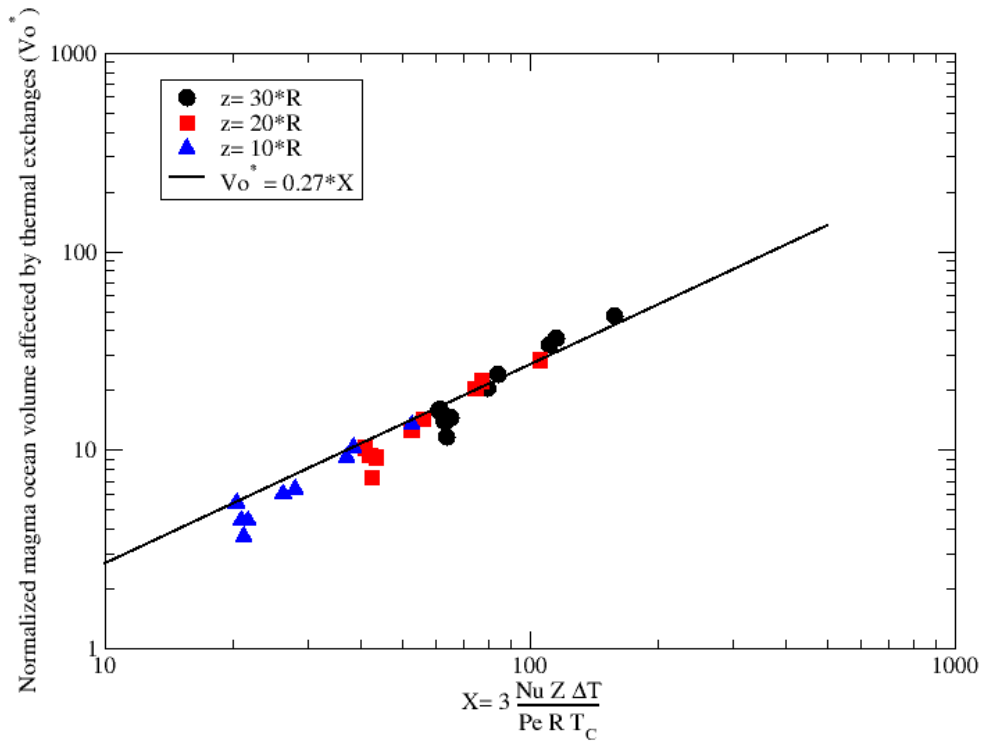


Figure 14: Dimensionless heated magma ocean volume as a function of  $X$ , and comparison with our scaling law (23). Our numerical results are represented with different symbols for different given depths.

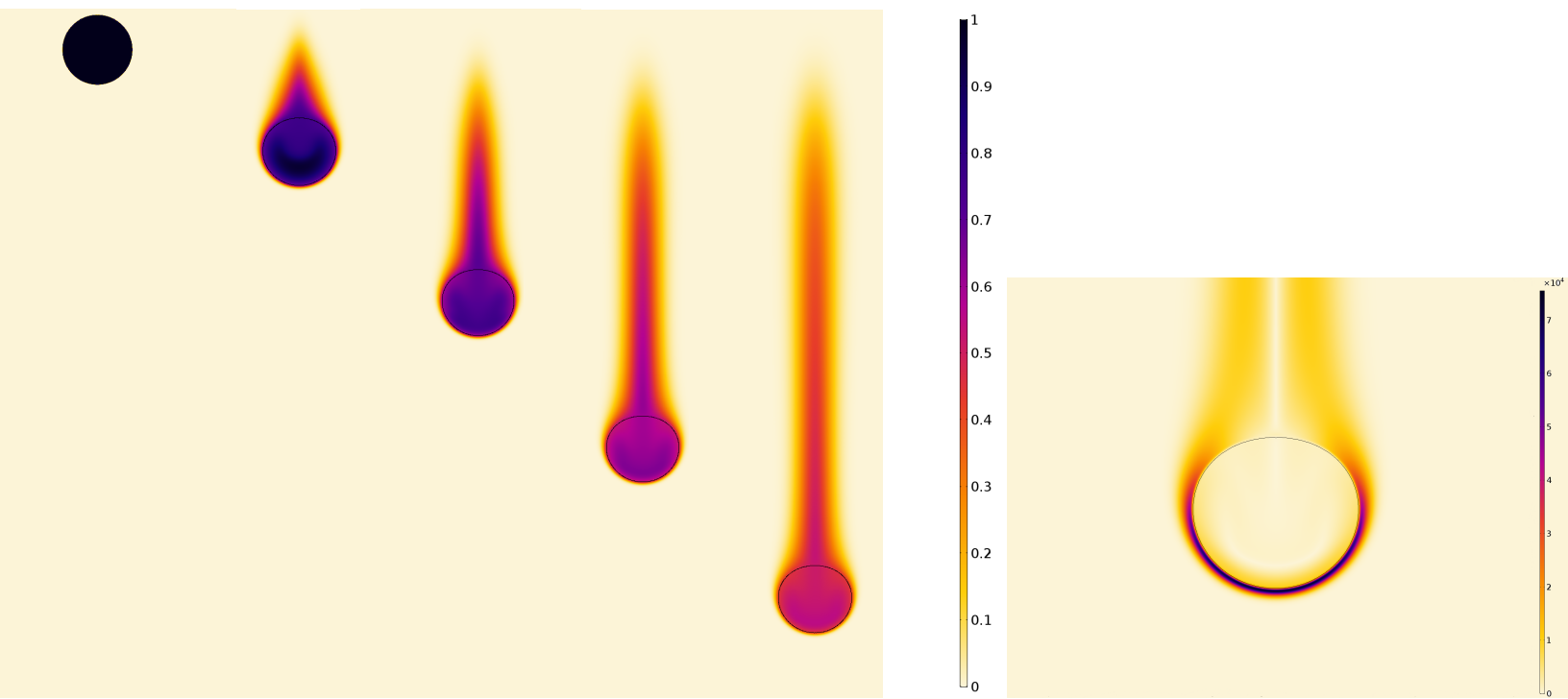


Figure 15: Thermal evolution of the non-deformable metal drop as a function of normalized time (Left). From left to right,  $t^*=0, 0.0167, 0.033, 0.05$  and  $0.067$ . The right figure shows the temperature gradient (K/m) in and around the spherical drop case. In this model,  $Re = 0.76$ ,  $Pe = 254$  and  $R_\mu=1000$  (simulation #3 in Table 2)

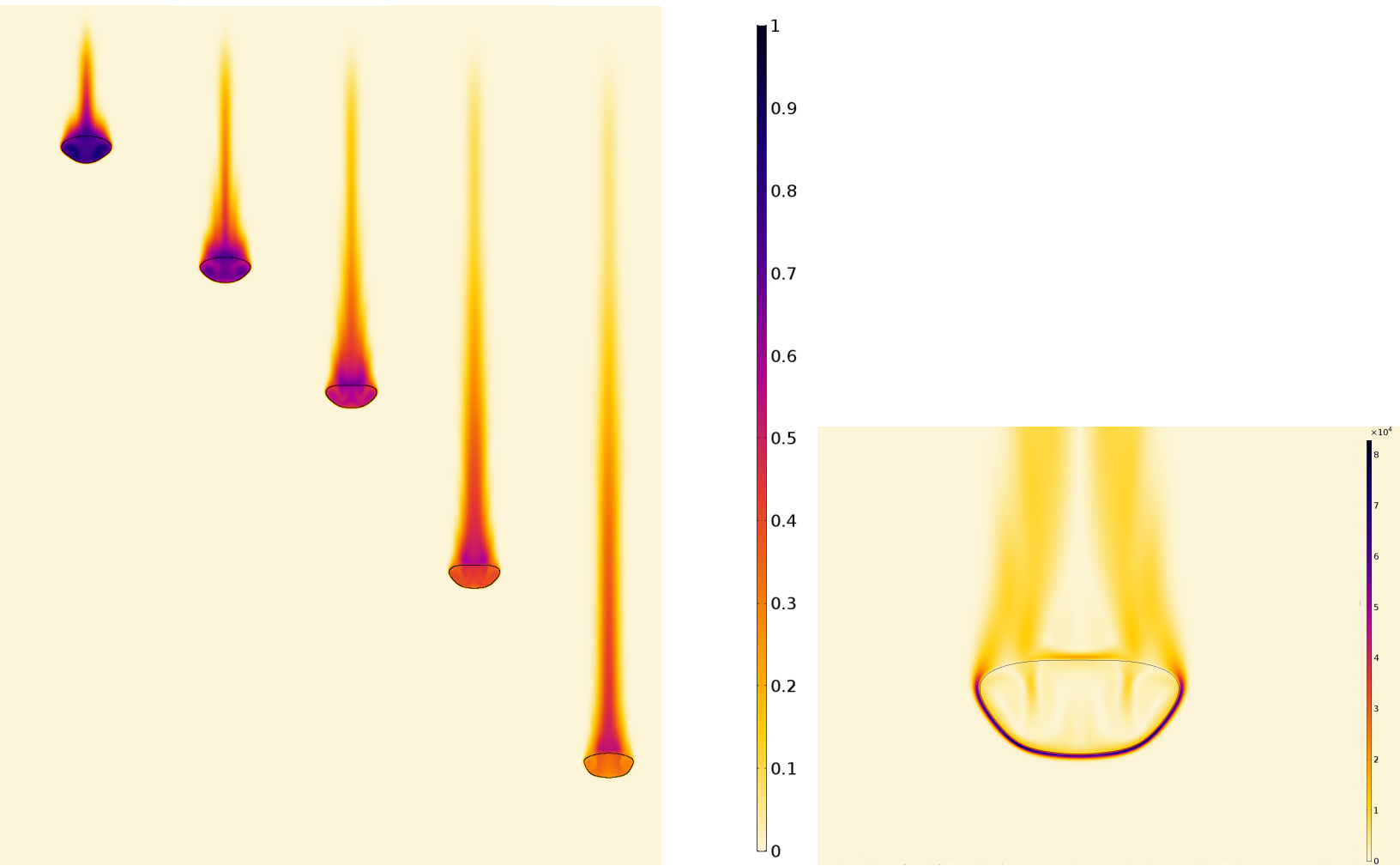


Figure 16: Thermal evolution of the weakly deformable metal drop as a function of normalized time (Left). From left to right,  $t^*=0.015, 0.024, 0.033, 0.047$  and  $0.06$ . The right figure shows the temperature gradient (K/m) in and around the deformable drop. In this model,  $Re = 21.8$ ,  $Pe = 728.36$  and  $R_\mu=100$  (simulation #5 in Table 2)

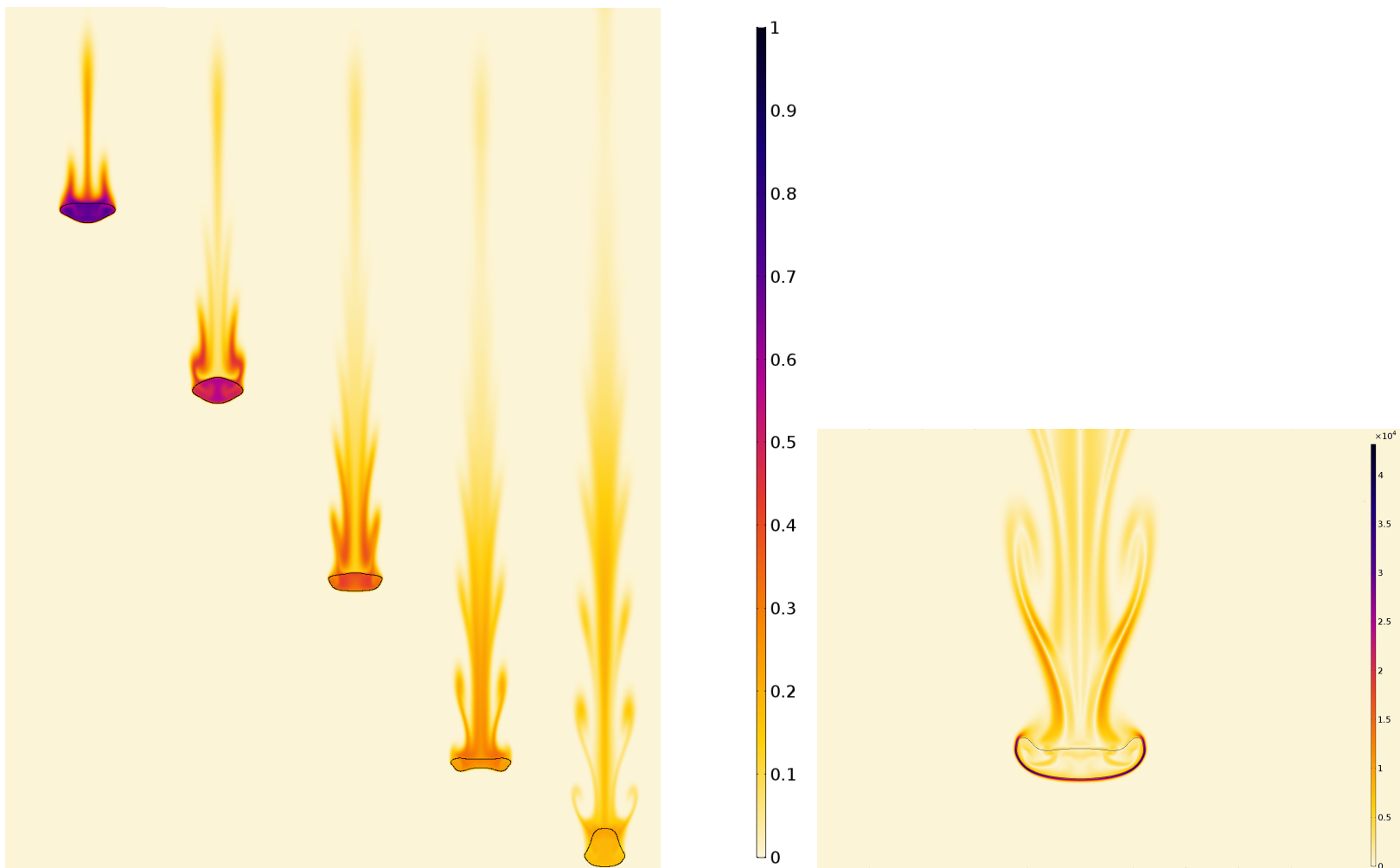


Figure 17: Thermal evolution of the strongly deformable metal drop as a function of normalized time (Left). From left to right,  $t^*=0.02, 0.033, 0.047, 0.06$  and  $0.077$ . The right figure shows the temperature gradient (K/m) in and around the deformable drop case. In this model,  $Re = 47.6$ ,  $Pe = 793.73$  and  $R_\mu=50$  (simulation #6 in Table 2)

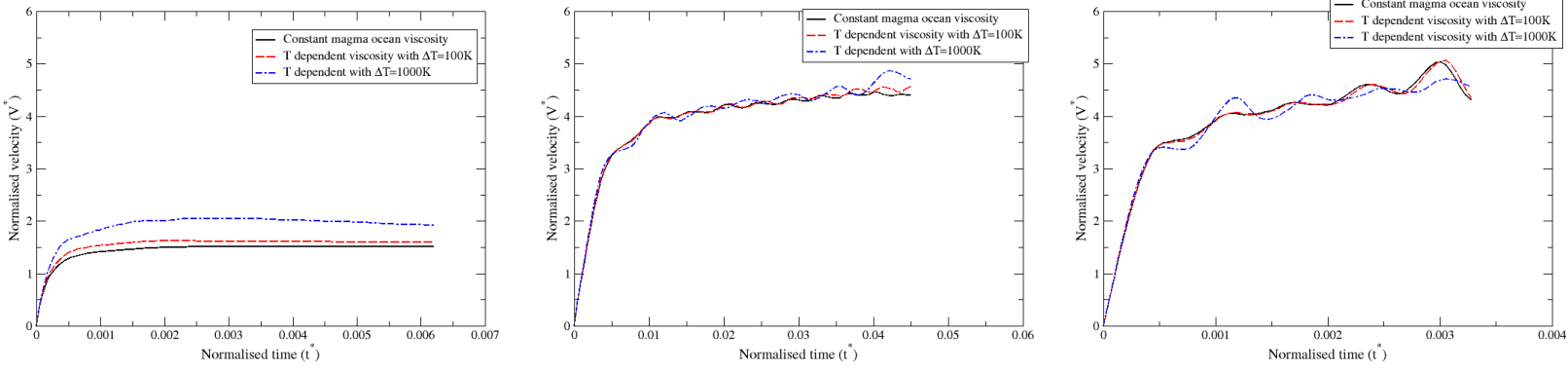


Figure 18: Comparison of the normalized average velocity field as a function of normalized time to show the influence of a temperature dependent viscosity for: a non-deformable spherical drop (Left), a weakly deformable drop (Middle) and a strongly deformable drop (Right). The black lines present the constant magma ocean viscosity. The red (blue) dashed lines present the temperature dependent viscosity with  $\Delta T = 100$  K ( $\Delta T = 1000$  K).

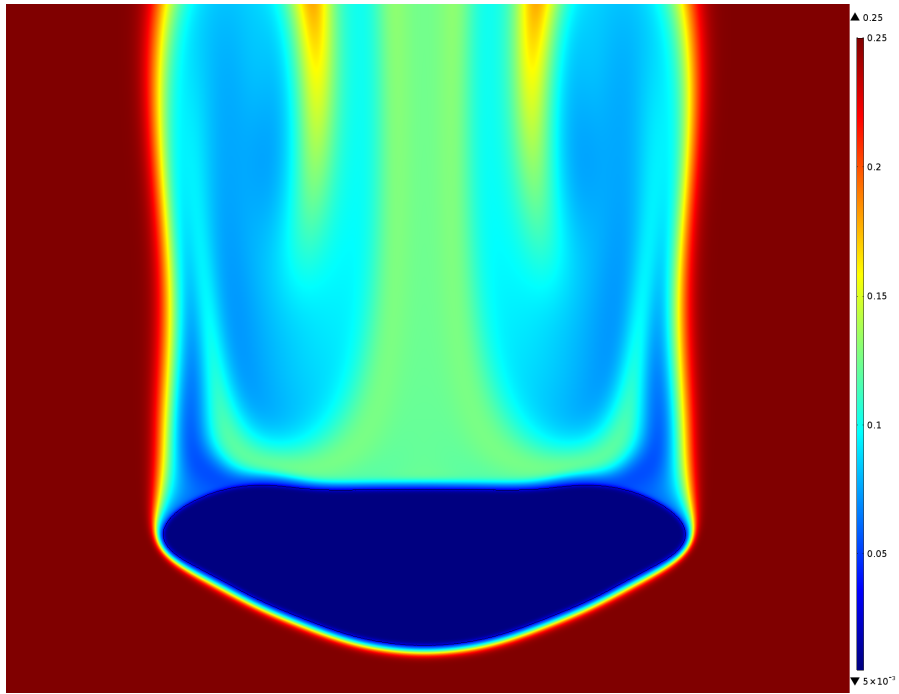


Figure 19: View of the viscosity field (in Pa.s) around the strongly deformable drop when a temperature dependent viscosity is considered.

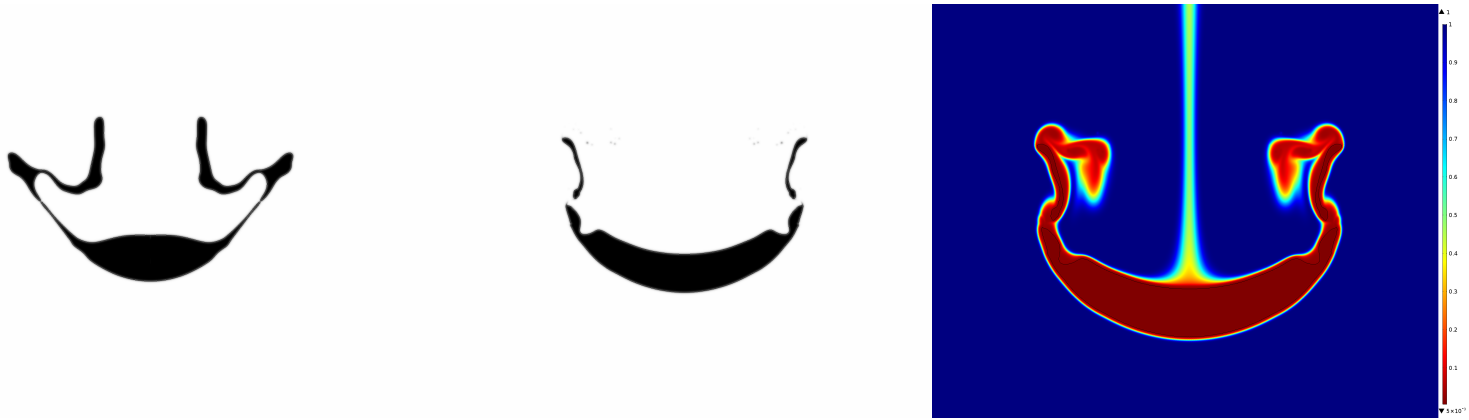


Figure 20: Final form at breaking of the drop for a constant viscosity magma ocean (Left) and a temperature dependent viscosity magma ocean (Middle). On the right, view of the viscosity field (in Pa.s) around the drop in the later case. In this model,  $Re = 50$ ,  $Pe = 3330$  and  $R_\mu=200$  (simulation #10 in Table 2).

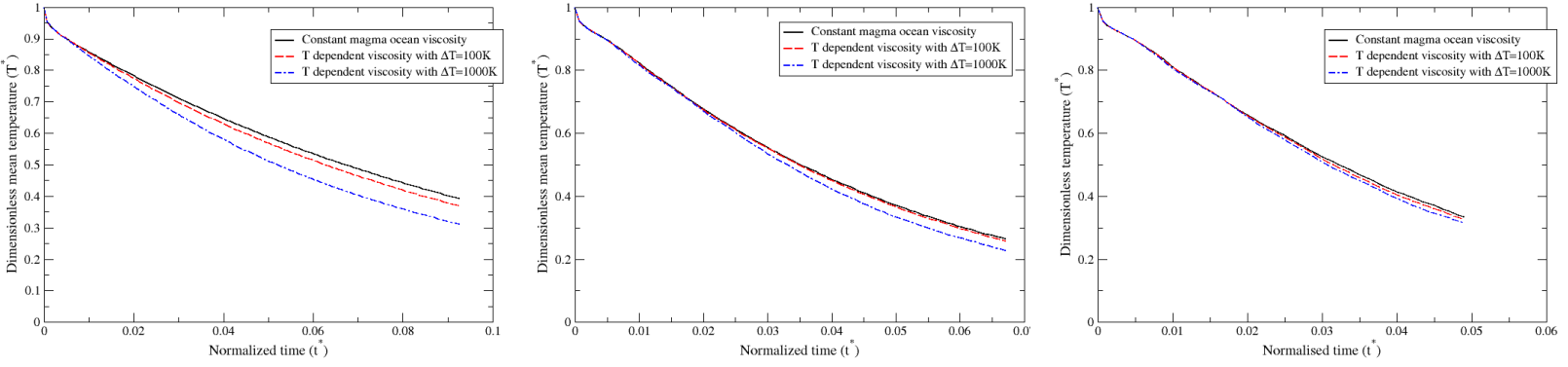


Figure 21: Comparison of the dimensionless temperature as a function of normalized time for a non-deformable drop (Left), a weakly deformable drop (Middle) and a strongly deformable drop (Right). The black lines present the constant magma ocean viscosity. The red (blue) dashed lines present the temperature dependent viscosity with  $\Delta T = 100\text{ K}$  ( $\Delta T = 1000\text{ K}$ ).

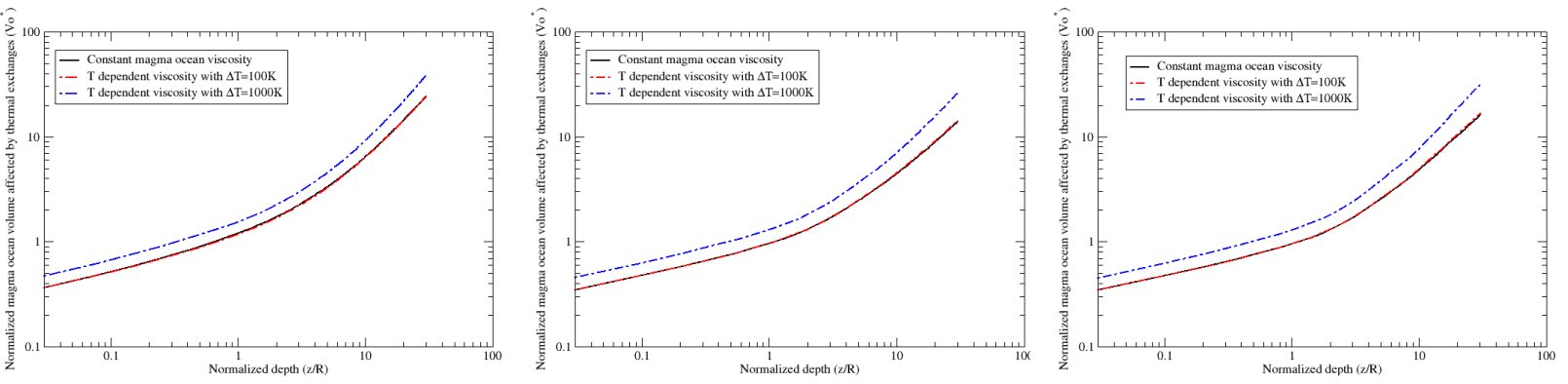


Figure 22: Comparison of normalized heated magma ocean volume as a function of normalized time for a non-deformable drop (Left), a weakly deformable drop (Middle) and a strongly deformable drop (Right). The black lines present the constant magma ocean viscosity. The red (blue) dashed lines present the temperature dependent viscosity with  $\Delta T = 100$  K ( $\Delta T = 1000$  K).